Chapter 3
Thermodynamics of Small Lennard-Jones Clusters

3.1 Introduction

Much of the interest in the thermodynamics of clusters has centred on the melting transition, particularly its character as the finite-size analogue of the bulk first-order phase transition. Cluster melting differs from bulk in a number of ways. First, the finite size of clusters causes 'rounding' of thermodynamic properties[124–126]. The cluster melting transition occurs over a temperature range, not a single temperature; heat capacity peaks are not δ-functions, but instead remain finite.

Secondly, phase separation does not occur in most small clusters (potassium chloride clusters may provide an exception[127]), because the energetic cost of the interface is too large. This leads to certain thermodynamic features which are peculiar to clusters. One is that an ensemble of clusters in the melting region is a mixture of solid-like and liquid-like clusters with the ratio fixed by the relative stabilities of the two forms. If one was to observe a single cluster, it would be seen to occasionally change form between solid-like and liquid-like[128,129]. There is a dynamic coexistence of the two states. These phase-like forms have different characteristic properties. For example, the liquid-like state has a higher potential energy, floppier vibrations, a more disordered structure, and a larger diffusion constant[130]. If these differences between states can be quantified using an order parameter, the presence of more than one state will give rise to multimodal probability distributions of that order parameter. Such multimodality can be related to the thermodynamic stability of the states through the concept of Landau functions[131,132], which describe the thermodynamic potential, i.e. the entropy (microcanonical ensemble) or the Helmholtz free energy (canonical ensemble), in terms of an order parameter. The presence of a first-order phase transition is indicated by two stable states of the Landau function, e.g. two minima in the Landau free energy separated by a barrier.

The order parameters that have been most successful in elucidating the nature of cluster melting have taken advantage of the differences in potential energy between the solid-like and liquid-like states[133]. The ability of the order parameter to distinguish between states can sometimes be enhanced by averaging the parameter over short times to reduce the vibrational broadening[112]. The short-time averaged (STA) temperature has proved to be a particular useful microcanonical order parameter[130]. For this time averaging to succeed the length of time the cluster resides in each state needs to be much longer than the time scale for vibrational motion.

Another unusual feature that results from the absence of phase separation for clusters is the possibility of Van der Waals loops (or S-bends) in the microcanonical caloric curve[134]; there can be a range of energy for which the cluster has a negative specific heat capacity[135–137]. The loops are a result of the transition from the high temperature, low potential energy solid-like state to the low temperature, high potential energy liquid-like state. In §3.7 we use an analytical model to investigate the conditions under which they are most likely to occur, examining in particular the effect of system size.

The standard way to calculate the thermodynamic properties of clusters is by some form of simulation, normally based on the Monte Carlo (MC) or molecular dynamics (MD) methods, perhaps augmented by more sophisticated techniques to help achieve ergodicity, such as jump-walking[138] or umbrella sampling[139], or to extract densities of states, such as the multi-histogram methods[140–142]. Such simulations give 'exact' results for the thermodynamics within the statistical errors of the simulation. An alternative route to calculate accurate densities of states is provided by Reinhardt's adiabatic switching method[143]; it has the advantage over histogram MC that it can extract absolute (not relative) values for the densities of states.

However, before such simulations became computationally feasible, considerable attention was given to the calculation of thermodynamic properties of clusters from the PES. Initially, calculations were performed in the harmonic approximation using only knowledge of the vibrational spectrum of a single low energy structure[10,11,144–146]. McGinty and Burton realized that if their results were to have relevance for more than low temperature behaviour, other configurations needed to be included in their partition function[10,145], but without the means to systematically search the PES they were unable to implement this extension of their approach. In particular, if this method is to model the melting transition, the large number of high potential energy minima associated with the liquid-like state need to be taken into account. Hoare and McInnes did obtain a suitable database of minima for small LJ clusters[64,65], and although they outlined the method by which the thermodynamic properties could be calculated from this sample[147], the results were never published. However, with the advent of reliable simulation methods and adequate computer power to carry them out, such calculations were neglected.

Interest in the relationship of the thermodynamics of clusters to the PES was rekindled by the application of Stillinger and Weber's inherent structure approach[148] to clusters. The basic idea is that every configuration of a system can be mapped onto a minimum of the PES (an 'inherent structure'), by a steepest-descent path or 'quench'. This mapping allows one to consider the thermodynamic effects of the energy spectrum of minima separately from thermal motion within the wells, and gives a clearer view of structure, especially for liquids, by removing vibrational noise. In the application of this method to clusters, the thermodynamic and dynamic properties were elucidated by relating them to the qualitative features of the PES, especially the low energy minima and saddle points, thus allowing an intimate connection to be made between structure and thermodynamics[108,130,149–151].

This relationship between cluster thermodynamics and the PES was further developed by Bixon and Jortner[152] who considered the thermodynamics that resulted from different model energy spectra of minima. They showed that a large energy gap between the global minimum and a manifold consisting of a large number of higher energy minima was necessary to produce a significant feature in the caloric curves.

The wheel finally returned to the ideas of Burton, McGinty and Hoare, when Wales[153] and Franke *et al.*[154] independently developed a method to quantitatively determine the thermodynamic properties from the PES. A sample of minima is generated by systematic quenching from a high energy MD run. $\Omega(E)$ is then calculated by summing the harmonic density of states for each minima. This approach has been called the harmonic superposition method, and has been applied to a number of cluster systems to obtain a wide variety of thermodynamic properties[133,155].

The main focus of this chapter is to extend the harmonic superposition method to incorporate anharmonicity (§3.5) and to show how this method can give added physical insights into the thermodynamics by allowing the roles of different regions of the PES to be quantitatively examined (§3.6). First though, we briefly outline the simulation methods that we have used both for LJ_{55} in §3.3 and for the Morse systems studied in Chapter 4. The results for LJ_{55} (§3.3) provide both an example of some of the typical features seen in cluster thermodynamics, and also some of the results necessary for the analysis in §3.5. We then briefly review the harmonic superposition method (§3.4), before addressing the extension of the method to include anharmonicity. Finally, we investigate the effect of size on the possibility of Van der Waals loops appearing in the microcanonical caloric curves (§3.7).

3.2 Simulation Methods

The potential used in this study was the Lennard-Jones form[83],

$$E = 4\,\epsilon \sum_{i<j} \left[\left(\frac{\sigma}{r_{ij}} \right)^{12} - \left(\frac{\sigma}{r_{ij}} \right)^{6} \right], \tag{3.1}$$

where r_{ij} is the distance between atoms i and j. With ϵ, σ and m as the units of energy, distance and mass, respectively, the unit of time is $(m\sigma^2/\epsilon)^{\frac{1}{2}}$. MD simulations of the microcanonical ensemble were conducted using the velocity Verlet algorithm[156]. The initial phase point had zero linear and angular momentum. To prevent evaporation the clusters were placed in a container with walls represented by a LJ type repulsion[153,157]. When an atom hit the wall of the container an equal and opposite force was exerted on the rest of the cluster to prevent linear momentum transfer. As the two forces are collinear, there is also no transfer of angular momentum. The effect of the box is to restrict the phase space considered to bound clusters. The time step used was 0.0465 reduced time units, which is equivalent to 1×10^{-14}s for Ar.

The relative root-mean-square interatomic separation δ was used to assess the degree of melting. It is defined as

$$\delta = \frac{2}{N(N-1)} \sum_{i<j} \frac{\sqrt{\left\langle R_{ij}^2 \right\rangle - \left\langle R_{ij} \right\rangle^2}}{\left\langle R_{ij} \right\rangle}, \tag{3.2}$$

where the angle brackets indicate that an average is taken over the whole trajectory. Lindemann's criterion[158] states that melting is expected when δ becomes greater than about 0.1.

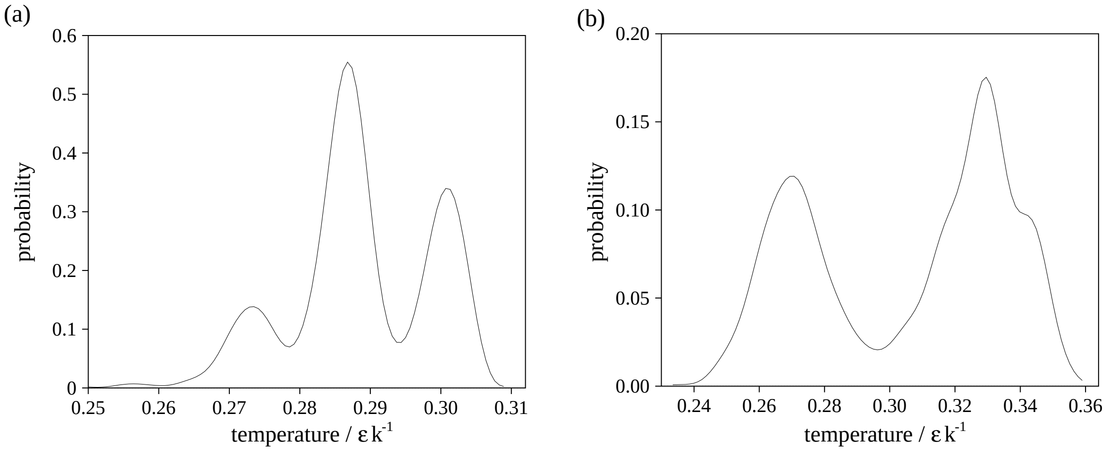

FIGURE 3.1: Probability distributions of STA temperatures for LJ_{55} from MD runs at (a) $54.243\,\epsilon$ and (b) $62.273\,\epsilon$ above the energy of the Mackay icosahedron, $-279.248\,\epsilon$.

The kinetic temperature is calculated from the kinetic energy, E_K, via the generalized equipartition theorem:

$$T_K = \frac{2E_K}{k(3N-6)} \tag{3.3}$$

by taking the mean of T_K over the whole trajectory. This expression is exact in the canonical ensemble, but T_K differs by $\mathcal{O}(N^{-1})$ from the thermodynamic definition of temperature (equation 3.10) in the microcanonical ensemble[159]. STA temperatures were found by averaging T_K over 500 time steps.

3.3 The 55-atom Lennard-Jones Cluster

LJ_{55} has been the focus of much study as an archetype for the melting of small clusters. It exhibits a clear Van der Waals loop and a large peak in the heat capacity[135]. If the potential energy is used as an order parameter, there is a range of energy for which two Landau free energy minima occur corresponding to the solid-like and liquid-like states[133]. If short time averaging is used more structure is revealed in the solid-like branch of the caloric curve. Before melting, atoms can pop out of the surface layer creating a vacancy and a mobile adatom[108,110,111,149]. This defect creation leads to enhanced diffusion in the surface layer, whilst the core of the cluster remains rigid.* Kunz and Berry observed that the cluster would spend a period of time in one region of configuration space, say with a

*Although this behaviour has been referred to as 'surface melting' in some studies[109–111] we prefer not to use this terminology because the behaviour does not evolve with increasing size to the surface melting familiar for bulk surfaces[160].

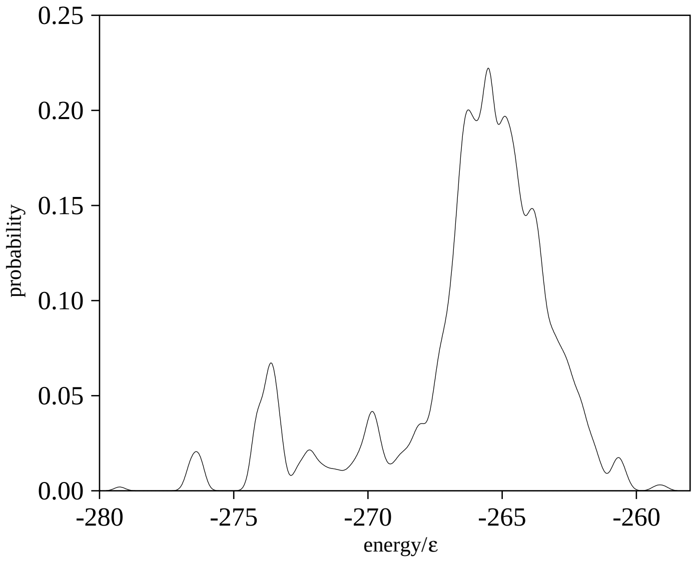

FIGURE 3.2: Probability distribution of the potential energy for a sample of 989 minima of LJ_{55}.

single surface vacancy, and then jump to a region with a different number of vacancies and a different characteristic potential energy. As a result, multimodality is seen in the probability distributions for the microcanonical STA temperature. An example is shown in Figure 3.1a where three coexisting states are seen. As the STA temperature reflects the minimum energy of the wells with which the cluster is associated (high temperatures correspond to low energy minima), we expect that the STA temperature peaks will be related to features in the energy distribution of minima (Figure 3.2).

To test this hypothesis, quenches were performed from configurations generated by an MD run at the energy of Figure 3.1a if they had an STA temperature near to the maxima of any of the three peaks. The resulting minima were then assigned to one of the six energy ranges given in Table 3.1. The results, given in Table 3.2, unequivocally show the correspondence between the STA temperature peaks and the peaks in the potential energy probability distribution for minima. Therefore the STA temperature can be used to elucidate the connection between the observed behaviour and local minima on the PES.

The highest temperature peak corresponds to the Mackay icosahedral global minimum, but to assign sets of structures to the other peaks, some of the minima in energy ranges II and III were examined further. Range II consists of icosahedral-based structures with a vacancy in a five-coordinate vertex site and a single adatom. There are eleven such structures, four with the adatom in the centre of a trian-

TABLE 3.1: Division of the of LJ_{55} PES into energy ranges based upon the features in the distribution of minima (Figure 3.2). There are no minima with energies between regions I and II, and II and III.

Region	Lower energy bound/ϵ	higher energy bound/ϵ
I	-279.24847	-279.24847
II	-276.60429	-276.19935
III	-274.50000	-273.00000
IV	-273.00000	-271.50000
V	-271.50000	-268.84000
VI	-268.84000	$-$

TABLE 3.2: Results of quenching from an MD run for LJ_{55} at an energy of $54.243\,\epsilon$ relative to the icosahedron.

Lower Temperature	Upper Temperature	Number of quenches	I	II	III	IV and V
0.3047	0.3050	110	110	0	0	0
0.2909	0.2912	72	2	70	0	0
0.2756	0.2785	86	1	9	74	2

gular face (Figure 3.3a) and seven with the adatom in an off-centre site (Figure 3.3b). These structures have been reported previously in a study using a more sophisticated potential to represent Ar[108]. Range III consists of structures with two vertex vacancies and two adatoms (Figure 3.3c–f and h–j), and structures with a vacancy in a six-coordinate edge site and a single adatom (Figure 3.3g). For the lower energy structures in this range, the two adatoms form a pair, either on the same face (Figure 3.3c and d) or straddling two faces (Figure 3.3e and f). We also examined some minima corresponding to range IV. We found structures with three adatoms, as well as some with adjacent edge and vertex vacancies and two adatoms (Figure 3.3k) and more complicated distorted icosahedra (Figure 3.3l).

To map out the microcanonical caloric curve MD runs each of 2.5×10^6 time steps were performed at 23 energies around the coexistence region. As expected the resulting curve has a Van der Waals loop. The STA temperature distributions were calculated for each energy. At low energies the distribution is unimodal, because the cluster remains in the Mackay icosahedral well. As it becomes possible

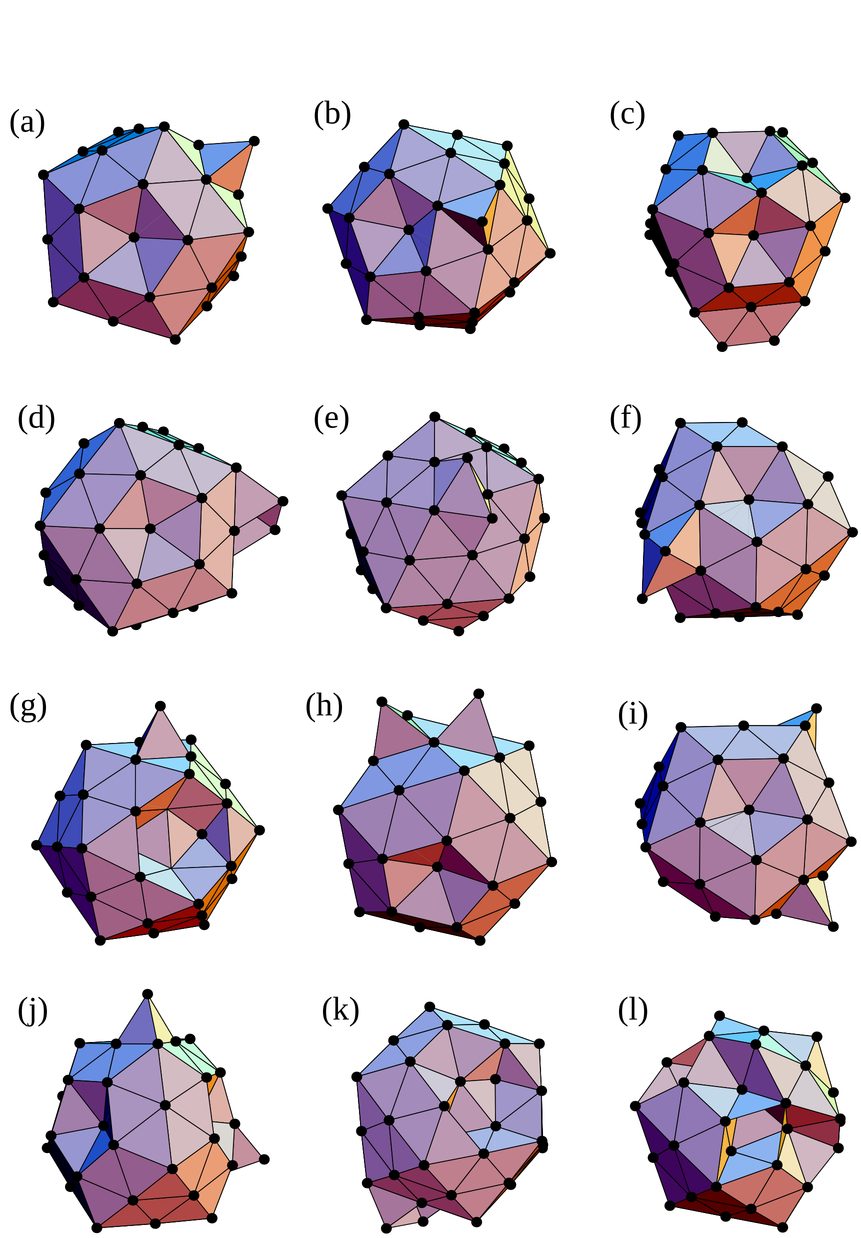

Figure 3.3: A selection of representative minima of LJ_{55} from energy ranges II, III and IV. Energies and point groups are given in Table 3.3.

to create surface vacancies, the distributions first become bimodal (at $48.193\,\epsilon$), and then trimodal (at $49.183\,\epsilon$). At $60.238\,\epsilon$ a much broader peak appears at lower temperature. Figure 3.1b shows this bimodal behaviour; it is due to dynamic coexistence between the liquid-like and solid-like states. The shoulders of the high-temperature peak are the remnants of the trimodal behaviour seen at lower energies. The peaks have merged because the greater vibrational energy has

TABLE 3.3: Energies of the LJ_{55} minima represented in Figure 3.3.

Label	Description	PG	Energy/ϵ
a	vertex vacancy + centred adatom	C_s	-276.59676
b	vertex vacancy + off-centred adatom	C_1	-276.19935
c	2 vertex vacancies + adatom pair	C_s	-274.28136
d	2 vertex vacancies + adatom pair	C_1	-274.25058
e	2 vertex vacancies + adatom pair	C_1	-274.21687
f	2 vertex vacancies + adatom pair	C_1	-274.13672
g	edge vacancy + centred adatom	C_s	-274.08950
h	2 vertex vacancies + 2 adatoms	C_1	-273.83234
i	2 vertex vacancies + 2 adatoms	C_1	-273.62356
j	2 vertex vacancies + 2 adatoms	C_1	-273.21257
k	fused vertex and edge vacancy + adatom pair	C_1	-272.82603
l	distorted icosahedron	C_s	-272.58659

broadened the temperature distributions for each state. The trimodal character of the high temperature peak would reappear if a longer averaging period was used.

The STA temperature distributions were partitioned according to their peaks, and the mean and standard deviation of the temperature were calculated for each, along with the integrated probabilities. This allows the caloric curves for restricted regions of the configuration space to be obtained (Figure 3.4a). Regions II and III have a small effect on the caloric curve; they cause it to bend gradually away from the temperature corresponding to the Mackay icosahedron alone. From the probabilities (Figure 3.4b) it can be seen that, despite their length, some of the MD runs have not achieved ergodicity in the energy range $47-55\,\epsilon$. This is because the free energy barriers between the different states can be large, and so passage between the different states can be infrequent on the time scale of the run.

3.4 The Harmonic Superposition Method

The total energy density of states associated with a single minimum on the PES is in the harmonic approximation[161]

$$\Omega(E) = \frac{(E - E^0)^{\kappa-1}}{\Gamma(\kappa)\prod_{j=1}^{\kappa} h\nu_j}\theta(E - E^0), \tag{3.4}$$

where E^0 is the potential energy of the minimum, θ is the Heaviside step function, and κ, the number of vibrational degrees of freedom, is $3N-6$. (As we will

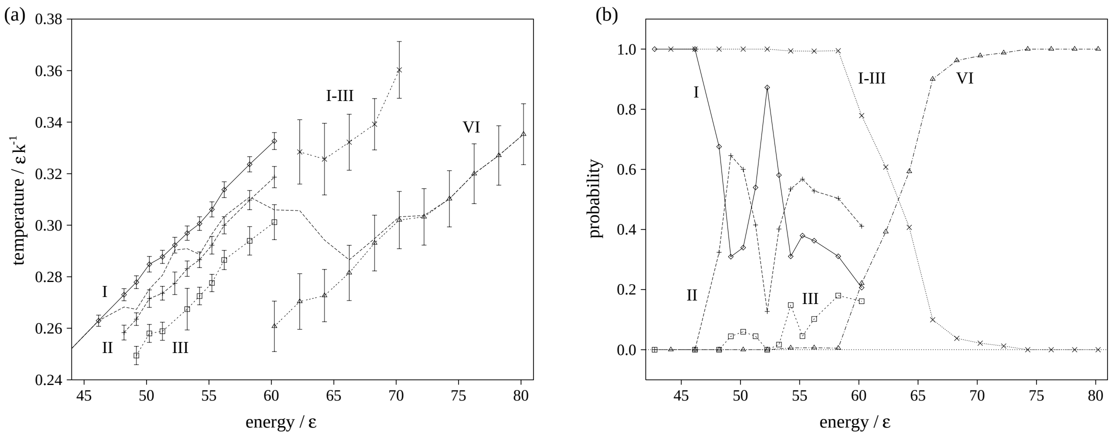

FIGURE 3.4: (a) Plot of the temperature against energy for LJ_{55}. The caloric curve has been split into contributions from regions of configuration space corresponding to peaks in the STA temperature distribution. The overall caloric curve is represented by the dashed line without any error bars. (b) Plot of the probability of LJ_{55} being in regions of phase space I, II, III and VI characterized by their different STA temperatures. Above $60\,\epsilon$ regions I–III were indistinguishable. The energy is measured relative to the energy of the global minimum icosahedron.

be comparing our results to those for stationary, non-rotating clusters, we do not include translational or rotational contributions to the density of states.) To calculate the density of states for the whole system, all the minima on the PES need to be considered. We make a superposition approximation and sum the density of states over all the minima low enough in energy to contribute. This approximation is equivalent to assuming that the phase space hyperellipsoids associated with each minimum do not overlap. This gives

$$\Omega(E) = \sum_{E_s^0 < E} \frac{n_s^*(E - E_s^0)^{\kappa-1}}{\Gamma(\kappa)\prod_{j=1}^{\kappa} h\nu_j^s}, \tag{3.5}$$

where the sum is over all the geometrically distinct minima on the surface; n_s^*, the number of permutational isomers of minimum s, is given by $n_s^* = 2N!/h_s$ where h_s is the order of the point group of s.†

The difficulty with equation 3.5 is that for all but the very smallest clusters this sum involves an impractically large number of minima. Hoare and McInnes[64], and more recently Tsai and Jordan[162] have enumerated lower bounds to the number of geometric isomers for LJ clusters from 6 to 13 atoms. This number rises

†In their formulation of the superposition method Hoare and McInnes missed out the effect of symmetry[147]. This explains why in the brief mention of the results that they obtained, the method predicted that for LJ_{13} the cluster would reside in the icosahedral global minimum up to a reduced temperature of 0.6. (LJ_{13} in fact melts at $\sim$0.29). Without the inclusion of symmetry, the density of the states of the icosahedron is overestimated by 120 times.

exponentially with N. Extrapolating this trend gives for LJ_{55} an estimate of 10^{21} geometric isomers. In such a case, as it is not possible to obtain a complete set of minima, a representative sample is needed. A large set of minima can be obtained by systematic quenching from a high energy MD trajectory. However, this gives a greater proportion of the low energy minima than of the high energy minima. Consequently, if the sample is used in equation 3.5 it is likely to underestimate the density of states due to the high energy minima, and so be inaccurate at high energies.

A method is needed which corrects for the incomplete nature of the sample of minima. This correction can be achieved by weighting the density of states for each known minimum by g_s, the number of minima of energy E_s^0 for which the minimum s is representative. Hence,

$$\Omega(E) = \sum_{E_s^0<E} \frac{g_s n_s^*(E-E_s^0)^{\kappa-1}}{\Gamma(\kappa)\prod_{j=1}^{\kappa} h\nu_j^s}, \tag{3.6}$$

where the sum is now over a representative sample of minima. The effect of g_s can be incorporated by using the quench statistics. If the system is ergodic and the MD run is performed at constant energy, the number of quenches to a minimum, γ, is assumed to be proportional to the density of states of the set of g_s minima, i.e. $\gamma(E')_s \propto g_s\Omega(E')_s$. Hence,

$$\begin{aligned} \Omega(E) &\propto \sum_{E_s^0<E} \gamma\left(E'\right)_s \frac{\Omega(E)_s}{\Omega(E')_s} &(3.7)\\ &\propto \sum_{E_s^0<E} \gamma\left(E'\right)_s \left(\frac{E-E_s^0}{E'-E_s^0}\right)^{\kappa-1}, &(3.8)\end{aligned}$$

where E' is the energy of the MD run. This reweighting technique is analogous to histogram Monte Carlo, but instead of determining the configurational density of states from the canonical potential energy distribution, g, effectively a density of minima, is found from the microcanonical probability distribution for quenching to a minimum.

If all the low energy minima are known, the n^* formula (equation 3.5) will be accurate at low energies. Therefore, the proportionality constant in the above equation can be found by matching it to the low energy form of the n^* formula. For LJ_{13} and LJ_{55}, the term due to the icosahedron is dominant at low energies, and other terms in the sum can be neglected. Comparing the first terms of equations

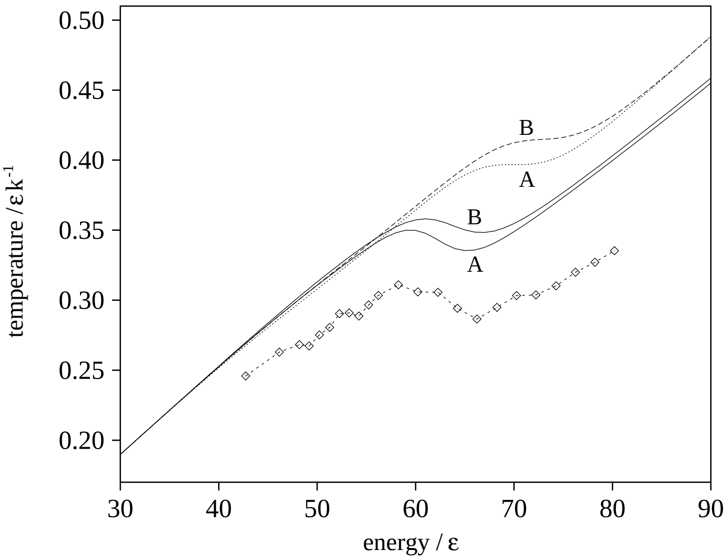

FIGURE 3.5: Microcanonical caloric curves for LJ_{55}. The solid lines were calculated from the γ formula, the dashed lines were calculated from the n^* formula, and the dashed line with diamonds shows the simulation results. The sample of minima used in the calculations is marked on the graph.

3.5 and 3.8 gives for the proportionality constant, c

$$c = \frac{n_0^*(E' - E_0^0)^{\kappa-1}}{\gamma\,(E')_0\,\Gamma(\kappa)\prod_{j=1}^{\kappa} h\nu_j^0}, \tag{3.9}$$

where E_0^0 is the energy of the global minimum.

A critical test of these formulae for $\Omega(E)$ is the predicted microcanonical caloric curve, which for LJ_{55} has a Van der Waals loop[135]. Using the thermodynamic definition of the microcanonical temperature, T_μ,

$$\frac{1}{kT_\mu} = \left(\frac{\partial \ln \Omega}{\partial E}\right)_{N,V} = \frac{1}{\Omega}\left(\frac{\partial \Omega}{\partial E}\right)_{N,V}, \tag{3.10}$$

an expression for T_μ can be derived[153]. For LJ_{55} we have two samples of minima produced by systematic quenching[153], details of which are given in Table 3.4. Sample A is from a MD run at an energy in the upper end of the coexistence region, and B at an energy just into the liquid-like region. The results for samples A and B using the n^* and γ formulations are given in Figure 3.5. It can be seen the n^* formula fails badly, predicting only an inflection in the caloric curve which is too high in energy. This failure is because the contribution to $\Omega(E)$ from the higher energy minima is underestimated. The γ formula is much more successful, reproducing the Van der Waals loop at the observed energy. That the harmonic superposition

TABLE 3.4: Details of the two samples of minima used for LJ_{55}. E' is measured with respect to the global minimum icosahedron.

	E'/ϵ	Number of minima
A	64.7485	989
B	70.2485	1153

method produces a caloric curve with the correct features shows, as Bixon and Jortner suggested[152], that the distribution of minima is crucial in determining the basic form of the caloric curve. However, the Van der Waals loop is too shallow and lies at too high a temperature. The discrepancy is due to the harmonic approximation. The temperature rises linearly with energy for a single harmonic well. The actual wells of the cluster, however, are flatter than assumed in the harmonic approximation, especially around the transition state regions. Consequently, the cluster spends more time in these high potential energy, low temperature regions of the PES, and so the true temperature is lower than that given by the harmonic approximation.

For smaller clusters it was found that the performance of the n^* formula improved[155]. This improvement occurs because there are fewer minima on the PES of a smaller cluster and so the set of minima obtained from quenching is more complete.

The harmonic superposition method has three main possible sources of error. The first is associated with the statistical accuracy of the quench frequencies. These errors can be mostly eliminated by having a long enough quench run to ensure ergodicity, and by choosing an appropriate energy for the MD run so that the relevant regions of phase space are all significantly sampled. When studying the thermodynamics of melting it is most appropriate to choose E' to lie in the coexistence region, as in the case of sample A, so that quenches to solid-like and liquid-like states are frequent. The second possible source of error is the assumption that the phase space volumes for each minima can be summed independently, i.e. the hyperellipsoids in phase space do not overlap. If overlap occurred $\Omega(E)$ would be overestimated. Of course, above an energy threshold the true phase space volumes of each minimum are interconnected, but this interconnection is normally due to the anharmonic extension of the phase volumes to form necks along the transition state valleys. The third possible source of error is the harmonic approximation. Near the bottom of the well this is a reasonable assumption, but as the energy is increased some parts of the well become increasingly flat. Consequently the harmonic approximation causes $\Omega(E)$ to be underestimated. Comparison of the caloric curves from simulation and the harmonic superposition method (Figure 3.5) shows that the harmonic superposition method does indeed underestimate $\Omega(E)$ and so the harmonic approximation is likely to be the main source of error.

3.5 Anharmonicity

Most attempts to model anharmonicity have concentrated on small systems. As the size of the system increases the difficulty increases greatly. For example, it would be impossible to do the necessary multi-dimensional phase space integrals in the definition of $\Omega(E)$,

$$\Omega(E) = \frac{1}{h^\kappa} \int\int \delta(H - E) dq^\kappa dp^\kappa. \tag{3.11}$$

Most approaches either attempt to calculate the anharmonic element using known information from the PES, such as the third and fourth derivatives of the potential at the minima and the dissociation energies[163] or assume the PES has a certain topology for which the partition function is known[164,165]. A normal mode approximation is often used because the multi-dimensional partition function is then the product of the one-dimensional normal mode partition functions. However, to then obtain the density of states the partition function must be inverse Laplace transformed. This procedure does not necessarily have an analytic solution, and so numerical methods sometimes have to be used[166,167].

The only attempt, that we know of, to evaluate analytically the anharmonic density of states of clusters is due to Chekmarev and Umirzakov[165]. Their expression contained a number of unknown parameters, which they had to estimate. This approximate approach was partly due to their lack of information about the PES of LJ_{13}, the cluster they considered. They showed their form was able to produce the types of feature seen in the LJ_{13} caloric curve, if not to reproduce it accurately. The approach we use here is similar. We are looking for a relatively simple method that will provide an analytical expression for the anharmonic contribution to $\Omega(E)$. We also want to examine how far it is possible to use information extracted from the PES in this task. We will focus on LJ_{55} as a test of the methods developed. For LJ_{55} we have a sample of 3481 transition states which were found from a random selection of 402 of the minima in sample B defined above[90]. We have also calculated the analytical third derivatives for this potential.

3.5.1 The effect of transition state valleys

Transition states are crucial to the dynamics of a system, but how much effect do they have on the thermodynamics? Associated with a transition state is a flat valley on the PES which connects two minima. These transition state valleys will make a contribution to $\Omega(E)$. To consider their effect we need an expression for the density of states of a transition state valley.

We write the partition function for the transition state valley as a product of a vibrational partition function for the $(\kappa - 1)$ modes orthogonal to the transition vector and a translational partition function for motion along the transition state valley. This separation gives

$$Z_{ts} = \frac{L}{h}\sqrt{\frac{2\pi m}{\beta}}\frac{e^{-\beta E_{ts}}}{\prod_{j=1}^{\kappa-1}\beta h\nu_j^{ts}}, \tag{3.12}$$

where L is the length of the transition state valley. Inverse Laplace transforming this expression gives for the density of states of the transition state valley,

$$\Omega(E)_{ts} = \frac{\sqrt{2\pi m}\,L\,(E - E_{ts})^{\kappa-\frac{3}{2}}}{h^{\kappa}\prod_{j=1}^{\kappa-1}\nu_j^{ts}\,\Gamma(\kappa-\frac{1}{2})}\,\theta(E - E_{ts}). \tag{3.13}$$

Our expression for the total density of states is then

$$\Omega(E) = \sum_{E_s^0<E}\frac{n_s^*}{h^{\kappa}}\left(\frac{(E-E_s^0)^{\kappa-1}}{\Gamma(\kappa)\prod_{j=1}^{\kappa}\nu_j^s} + \frac{\sqrt{2\pi m}}{\Gamma(\kappa-\frac{1}{2})}\sum_{E_s^0+\Delta_{s,t}<E}\frac{\sigma_{s,t}L_{s,t}(E-E_s^0-\Delta_{s,t})^{\kappa-\frac{3}{2}}}{\prod_{j=1}^{\kappa-1}\nu_j^{s,t}}\right), \tag{3.14}$$

where $\Delta_{s,t}$ is the barrier height of transition state t from minimum s, and the reaction path degeneracy $\sigma_{s,t} = h_s/h_t$ or $2h_s/h_t$ for non-degenerate and degenerate rearrangement mechanisms, respectively[168]. A degenerate transition state connects different permutational isomers of the same minimum. In the γ formulation we now have

$$\Omega(E) = \sum_{E_s^0<E}\gamma(E')_s\frac{\frac{(E-E_s^0)^{\kappa-1}}{\Gamma(\kappa)\prod_{j=1}^{\kappa}\nu_j^s} + \frac{\sqrt{2\pi m}}{\Gamma(\kappa-\frac{1}{2})}\sum_{E_s^0+\Delta_{s,t}<E}\frac{\sigma_{s,t}L_{s,t}(E-E_s^0-\Delta_{s,t})^{\kappa-\frac{3}{2}}}{\prod_{j=1}^{\kappa-1}\nu_j^{s,t}}}{\frac{(E'-E_s^0)^{\kappa-1}}{\Gamma(\kappa)\prod_{j=1}^{\kappa}\nu_j^s} + \frac{\sqrt{2\pi m}}{\Gamma(\kappa-\frac{1}{2})}\sum_{E_s^0+\Delta_{s,t}<E'}\frac{\sigma_{s,t}L_{s,t}(E'-E_s^0-\Delta_{s,t})^{\kappa-\frac{3}{2}}}{\prod_{j=1}^{\kappa-1}\nu_j^{s,t}}}. \tag{3.15}$$

Geometrically, the phase volume associated with the transition state valley is an elliptical hypercylinder. There is also a term due to the phase space overlap of this hypercylinder with the hyperellipsoid associated with the minimum. It can be evaluated[169], however it is a small term and so we neglect it, especially as initially we are only trying to determine the magnitude of the effect of the transition state valleys.

The set of transition states previously calculated is not an exhaustive set for the sample of minima. Its incompleteness could cause an underestimation of the density of states arising from the transition state valleys. We therefore performed a more exhaustive search for transition states from 13 minima representing a wide range of energies. This search indicated that a reasonable estimate of the average number of low energy transition states per minimum was 20 (not counting permutational isomers). For each minimum the density of states of the known transition state valleys was multiplied by $20/n_{ts}^s$, where n_{ts}^s is the number of known transition states for minimum s. If the sample of transition states contained none connected to a particular minimum, it was assigned 20 transition states with the average barrier height and average frequency. The length of the transition state valley was estimated using

$$L_{s,t} = D_{s,t} - \frac{1}{2\pi\overline{\nu^s}}\sqrt{\frac{2\Delta}{m}}, \tag{3.16}$$

where $D_{s,t}$ is the displacement in configuration space between minimum s and transition state t, and $\overline{\nu^s}$ is the average normal mode frequency of s. The second term is the average radius of the harmonic well in configuration space at an energy Δ above the minimum.

From the expression for $\Omega(E)$ in equation 3.15 the temperature can be calculated using equation 3.10. It can be seen from the microcanonical caloric curves given in Figure 3.6 that the transition state valleys cause the caloric curve to bend away from the harmonic curve and the Van der Waals loop to be displaced downwards, but these effects are small. Even if the number of transition states connected to a minimum is assumed to be greater than 20 the effects are only slightly increased. The addition of the density of states of the transition state valleys only accounts for a small part of the difference between the harmonic and the true caloric curves. This result occurs not because the contribution of the transition state valleys to the density of states is small compared to that of the minima—in fact the transition state valleys make a larger contribution than the minima above about 55ϵ. Rather it occurs because the density of states for the transition state valleys is not very different from that of the minima; the valleys are modelled as harmonic in all but one dimension. We therefore conclude that a method of modelling the anharmonicity of the wells on the PES is needed to

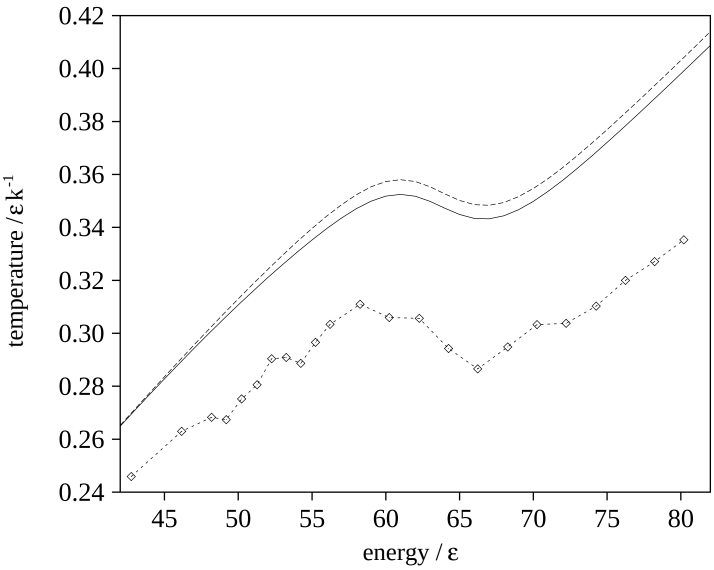

FIGURE 3.6: Microcanonical caloric curves for LJ_{55} using the γ formula with (solid line) and without (dashed line) the contribution from transition state valleys for sample A. The calculated caloric curve is compared to simulation (dashed line with diamonds).

obtain an accurate $\Omega(E)$. This agrees with Stillinger and Stillinger's conclusion that intrawell anharmonicity is dominant for LJ_{55} based on the fact that the caloric curve significantly deviates from the harmonic form at energies where the cluster always resides in the icosahedral well[108].

3.5.2 The effect of well anharmonicity

Here we follow the method of Haarhoff[164,166] to calculate an anharmonic correction term to the density of states. The energy levels for a Morse oscillator are given by

$$E = (n + \frac{1}{2})h\nu - (n + \frac{1}{2})^2 \frac{(h\nu)^2}{4D_e}. \tag{3.17}$$

This quadratic can be solved for n. The root corresponding to a bound state is

$$n + \frac{1}{2} = \frac{2D_e}{h\nu}\left(1 - \sqrt{1 - \frac{E}{D_e}}\right). \tag{3.18}$$

Assuming n is continuous and differentiating with respect to E gives a classical density of states,

$$\begin{aligned} \Omega(E) &= \frac{dn}{dE} = \frac{1}{h\nu\sqrt{1 - \frac{E}{D_e}}} \\ &= \frac{1}{h\nu}\left(1 + \frac{E}{2D_e} + \frac{3}{8}\left(\frac{E}{D_e}\right)^2 + \cdots\right), \end{aligned} \tag{3.19}$$

where the square root has been expanded binomially. The expansion is valid if E/D_e is small. The first term in the series is the harmonic term. The full series will diverge as $E \to D_e$. This divergence is the correct behaviour for the Morse oscillator, but for the case of a cluster isomerization $\Omega(E)$ remains finite as $E \to \Delta$ from below, where Δ is the barrier height. As we are seeking a correction term for well anharmonicity, it seems reasonable to truncate equation 3.19 and examine the effect of the first term in this series. Laplace transformation then gives for the partition function

$$z = \frac{1}{h\nu}\left(\frac{1}{\beta} + \frac{1}{2\Delta\beta^2}\right). \tag{3.20}$$

The multi-dimensional partition function is then

$$Z = \prod_{j=1}^{\kappa} \frac{1}{\beta h\nu_j}\left(1 + \frac{1}{2\Delta_j\beta}\right). \tag{3.21}$$

Making the approximation that an average value of $1/\Delta$ can be used then gives

$$Z = \frac{1}{\prod_{j=1}^{\kappa} h\nu_j} \sum_{l=0}^{\kappa} \frac{C_l^\kappa a^l}{\beta^{\kappa+l}}, \tag{3.22}$$

where $a = \langle 1/2\Delta \rangle$ is an anharmonicity parameter and C_l^κ is a binomial coefficient. Inverse Laplace transforming gives

$$\Omega(E) = \frac{1}{\prod_{j=1}^{\kappa} h\nu_j} \sum_{l=0}^{\kappa} \frac{C_l^\kappa a^l E^{\kappa+l-1}}{\Gamma(\kappa+l)}. \tag{3.23}$$

The total density of states is found by summing over all the minima, giving

$$\Omega(E) = \sum_{E_s^0<E} \frac{n_s^*}{\prod_{j=1}^{\kappa} h\nu_j^s} \sum_{l=0}^{\kappa} \frac{C_l^\kappa a_s^l (E-E_s^0)^{\kappa+l-1}}{\Gamma(\kappa+l)}. \tag{3.24}$$

Converting the above equation to the γ formulation using equation 3.7 gives

$$\Omega(E) \propto \sum_{E_s^0<E} \gamma(E')_s \left[\sum_{l=0}^{\kappa} \frac{C_l^\kappa a_s^l (E-E_s^0)^{\kappa+l-1}}{\Gamma(\kappa+l)} \Big/ \sum_{l=0}^{\kappa} \frac{C_l^\kappa a_s^l (E'-E_s^0)^{\kappa+l-1}}{\Gamma(\kappa+l)}\right]. \tag{3.25}$$

The temperature follows from equation 3.10

$$T_\mu = \frac{\displaystyle\sum_{E_s^0<E} \gamma(E')_s \left[\sum_{l=0}^{\kappa} \frac{C_l^\kappa a_s^l (E-E_s^0)^{\kappa+l-1}}{\Gamma(\kappa+l)} \Big/ \sum_{l=0}^{\kappa} \frac{C_l^\kappa a_s^l (E'-E_s^0)^{\kappa+l-1}}{\Gamma(\kappa+l)}\right]}{\displaystyle k\sum_{E_s^0<E} \gamma(E')_s \left[\sum_{l=0}^{\kappa} \frac{C_l^\kappa a_s^l (E-E_s^0)^{\kappa+l-2}}{\Gamma(\kappa+l-1)} \Big/ \sum_{l=0}^{\kappa} \frac{C_l^\kappa a_s^l (E'-E_s^0)^{\kappa+l-1}}{\Gamma(\kappa+l)}\right]}. \tag{3.26}$$

This anharmonic correction has a similar form to that used by Chekmarev and Urmirzakov[165] but has been derived in a different way.

We consider two possible ways of calculating a_s from the potential energy surface of LJ_{55}. Firstly, we consider using the third derivatives of the potential. The dissociation energy of a one-dimensional Morse oscillator can be found from the second and third derivatives of the potential by

$$D_e = \frac{(V'')^3}{(V''')^2}. \tag{3.27}$$

If off-diagonal elements in the multidimensional case are ignored, the above equation can be used to calculate the barrier heights associated with each normal mode. Using analytical third derivatives of the LJ potential, the Cartesian third derivatives for the LJ_{55} icosahedron were calculated and transformed to obtain the diagonal elements in the Hessian eigenvector basis. This scheme underestimates the anharmonicity and gives values for a_s which when substituted into equation 3.26 have an insignificant effect on $\Omega(E)$, because the off-diagonal elements, which far outnumber the diagonal elements, should not be neglected. However, there is no obvious way to calculate the effect of the off-diagonal elements and for a system such as LJ_{55} the transformation of the third derivatives into the Hessian eigenvector basis is too computationally expensive for the off-diagonal elements.

The second method considered was to use the barrier heights of our transition state sample. An average barrier height was calculated for each minimum, but for some minima it led to a gross overestimation of the anharmonicity and unphysical caloric curves. The barrier heights are not a good quantitative measure of the anharmonicity of an individual minimum. This method was therefore not considered further.

Therefore, instead of trying to obtain a_s from the PES, we considered how it could be obtained by comparison with the simulation results. If a_s is assumed to be the same for all minima, a value of a can be found which leads to the reproduction of the Van der Waals loop in the caloric curve at the observed temperature and energy, but the temperature difference between the two turning points is still too small. However, one would expect the anharmonicity to depend upon the energy of the minimum: the higher energy minima are likely to have a greater anharmonicity than the solid-like minima.

In §3.3, we saw an example of how the properties of different regions of configuration space could be obtained using suitable order parameters. Indeed, for LJ_{55}, the caloric curves associated with minima in different energy ranges were found. Using the superposition method, it is easy to calculate the properties of

TABLE 3.5: Values of the anharmonicity parameter, a_i, for LJ_{55} in the six energy ranges given in Table 3.1. Values for I, II, III and VI were found by fitting the temperatures for these regions to the simulation results.

Region	a_i/ϵ^{-1}
I	0.50
II	0.51
III	0.53
IV	0.65
V	0.70
VI	0.73

a particular region of configuration space simply by restricting the summation to those minima with suitable values of an order parameter, i.e.

$$\Omega_i = \sum_{E_s^0<E, s\in i} \Omega_s, \tag{3.28}$$

where Ω_i is the densities of states associated with region i. From the definition, $1/kT_i = (\partial \ln \Omega_i/\partial E)_{N,V}$, where T_i is the temperature of region i, it follows that

$$T_i = \frac{\displaystyle\sum_{E_s^0<E, s\in i} \gamma(E')_s \left[\sum_{l=0}^{\kappa} \frac{C_l^\kappa a_s^l (E-E_s^0)^{\kappa+l-1}}{\Gamma(\kappa+l)} \Big/ \sum_{l=0}^{\kappa} \frac{C_l^\kappa a_s^l (E'-E_s^0)^{\kappa+l-1}}{\Gamma(\kappa+l)} \right]}{\displaystyle k \sum_{E_s^0<E, s\in i} \gamma(E')_s \left[\sum_{l=0}^{\kappa} \frac{C_l^\kappa a_s^l (E-E_s^0)^{\kappa+l-2}}{\Gamma(\kappa+l-1)} \Big/ \sum_{l=0}^{\kappa} \frac{C_l^\kappa a_s^l (E'-E_s^0)^{\kappa+l-1}}{\Gamma(\kappa+l)} \right]}. \tag{3.29}$$

We assigned values of the anharmonicity parameter, a_i, to minima in the six different energy ranges (Table 3.1). Values were chosen for regions I, II, III and VI which reproduced the simulation results of Figure 3.4. The caloric curves for each region accurately fitted the simulation curves showing that our anharmonic correction term has an appropriate form. Values of a_i for regions IV and VI were chosen that were intermediate between the values for regions III and VI, but as these regions only make a small contribution to $\Omega(E)$ the exact value chosen will only have a very small effect on the overall caloric curve. The values of a_i are given in Table 3.5. As would be expected the anharmonicity increases with the potential energy of the minima.

The microcanonical caloric curve was calculated using these values of a_i. Figure 3.7 shows that for sample A the calculated curve is in remarkable agreement with the simulation results. The calculated Van der Waals loop now has the correct

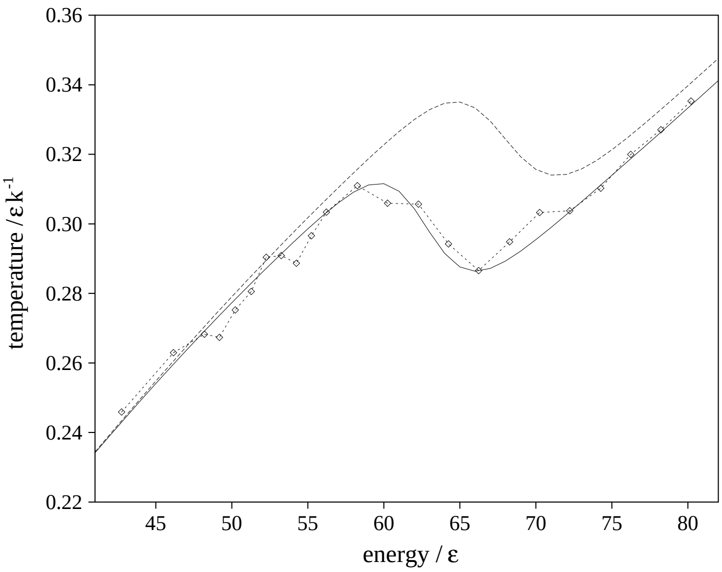

FIGURE 3.7: Microcanonical caloric curves for LJ_{55} using the γ formula including anharmonic terms with minima samples A (solid line) and B (dashed line). The calculated caloric curves are compared to simulation (dashed line with diamonds).

depth, because the effect of the greater anharmonicity of the liquid-like state is to increase the difference in temperature between the two branches of the caloric curve. The success of this method can be understood from the equation

$$\frac{1}{T} = \sum_i \frac{p_i}{T_i}, \tag{3.30}$$

where p_i is the probability that the cluster is in region i. The probabilities at E', $p_i(E')$ are fixed by the quench frequencies,

$$p_i(E') = \frac{\sum_{s\in i} \gamma_s(E')}{\sum_s \gamma_s(E')} \tag{3.31}$$

Furthermore, the p_i calculated from sample A are in good agreement with simulation results over a wide range of energy (see §3.6). The values of a_i have been chosen to reproduce the simulation temperatures, T_i, and so it is unsurprising that the overall temperature, T, is very accurate. Sample B produces worse results because there are fewer quenches to regions I–III, and so the quench frequencies are subject to larger statistical errors than for sample A.

For LJ_{13}, the STA temperature distribution is bimodal. The high temperature peak corresponds to solid-like clusters associated with the icosahedral global minimum, and the low temperature peak to liquid-like clusters. The residence times in the solid-like and liquid-like states are much shorter than for LJ_{55} and so the information provided by short-time averaging for LJ_{13} is less well-resolved. We partitioned the minima distribution into these two regions, and assigned values of a_i to each. The values of a_i were higher than for LJ_{55} and the curvature of the T_i curves differed from the simulation results. The apparently greater anharmonicity can be explained by the larger number of surface atoms for LJ_{13}. The incorrect curvature suggests that the energy dependence of the density of states is inappropriate and so the 2nd-order Morse correction term to the density of states was included. The resulting T_i curves fitted the simulation results much more accurately. The partition function for a single minimum including this term is

$$\begin{aligned} Z &= \prod_{j=1}^{\kappa} \frac{1}{\beta h \nu_j} \left(1 + \frac{a}{\beta} + 3 \left(\frac{a}{\beta} \right)^2 \right)^{\kappa} & (3.32) \\ &= \frac{1}{\prod_{j=1}^{\kappa} h\nu_j} \sum_{l=0}^{\kappa} \sum_{m=0}^{\kappa-l} D_{l,m}^{\kappa} \frac{3^m a^{l+2m}}{\beta^{\kappa+l+2m}}, & (3.33) \end{aligned}$$

where

$$D_{l,m}^{\kappa} = \frac{\kappa!}{l!m!(\kappa-l-m)!}. \qquad (3.34)$$

Inverse Laplace transforming and summing over all minima gives for the total density of states,

$$\Omega(E) = \sum_{E_s^0 < E} \frac{n_s^*}{\prod_{j=1}^{\kappa} h\nu_j^s} \sum_{l=0}^{\kappa} \sum_{m=0}^{\kappa-l} \frac{D_{l,m}^{\kappa} 3^m a_s^{l+2m} (E - E_s^0)^{\kappa+l+2m-1}}{\Gamma(\kappa+l+2m)}. \qquad (3.35)$$

In an MD simulation one calculates the kinetic temperature, T_K. For LJ_{55} the difference between the thermodynamic and kinetic temperatures is negligible. For LJ_{13} it is still small but not insignificant, and so T_K rather than T_μ is fitted to the simulation results. Bixon and Jortner found both temperatures produced very similar results in their model calculations of the microcanonical caloric curve[152]. T_K has been obtained for the harmonic superposition method by Franke *et al.* using the equipartition theorem[154], however this approach cannot be extended to include anharmonicity. We obtain T_K by a different method. Firstly we note that

$$\begin{aligned} \langle E_K \rangle &= \int_0^E p(E_K) E_K dE_K & (3.36) \\ &= \frac{1}{\Omega(E)} \int_0^E E_K \Omega_c(E - E_K) \Omega_K(E_K) dE_K, & (3.37) \end{aligned}$$

where $\Omega_K(E_K)$ is the kinetic density of states, $\Omega_c(E_c)$ is the configurational density of states, and the potential energy E_c is given by $E_c = E - E_K$. Deconvoluting $\Omega_K(E_K)$ from $\Omega(E)$ gives

$$\Omega_c(E_c) = \frac{1}{(2\pi m)^{\kappa/2} \prod_{j=1}^{\kappa} \nu_j} \sum_{l=0}^{\kappa} \sum_{m=0}^{\kappa-l} \frac{D_{l,m}^{\kappa} 3^m a_s^{l+2m} (E_c - E_s^0)^{\kappa/2+l+2m-1}}{\Gamma(\kappa/2+l+2m)}. \qquad (3.38)$$

TABLE 3.6: Details of the two samples of minima for LJ_{13}. E' is measured with respect to the global minimum icosahedron.

	E'/ϵ	Number of minima
C	13.7768	95
D	18.3268	295

TABLE 3.7: Values of the anharmonicity parameter, a_i, for the solid-like (I) and liquid-like (II) regions of the LJ_{13} PES. Region I is the potential well of the icosahedron and region II consists of all other minima.

Region	a_i/ϵ^{-1}
I	0.470
II	0.625

Integrating equation 3.37, summing over all minima and substituting into equation 3.3 gives

$$T_K = \frac{\displaystyle\sum_{E_s^0<E} \frac{n_s^*}{\prod_{j=1}^{\kappa} \nu_j^s} \sum_{l=0}^{\kappa} \sum_{m=0}^{\kappa-l} \frac{D_{l,m}^{\kappa} 3^m a_s^{l+2m} (E-E_s^0)^{\kappa+l+2m}}{\Gamma(\kappa+l+2m+1)}}{\displaystyle k \sum_{E_s^0<E} \frac{n_s^*}{\prod_{j=1}^{\kappa} \nu_j^s} \sum_{l=0}^{\kappa} \sum_{m=0}^{\kappa-l} \frac{D_{l,m}^{\kappa} 3^m a_s^{l+2m} (E-E_s^0)^{\kappa+l+2m-1}}{\Gamma(\kappa+l+2m)}}. \tag{3.39}$$

Sample C (Table 3.6) was used to calculate the caloric curve of LJ_{13} for the γ formulation because it was produced from an MD run in the coexistence region and so should have more accurate quench statistics for the low energy minima, and sample D was used for the n^* formulation because it is from the liquid-like region and so has a larger sample of minima. The values of a_i assigned to solid-like and liquid-like clusters are given in Table 3.7. From Figure 3.8 it can be seen that the caloric curve given by the n^* formulation agrees very well with simulation, because it is possible to obtain a near-complete set of minima for LJ_{13}. (Tsai and Jordan found 1328 minima in a comprehensive search of the LJ_{13} PES[162]. Many of these, though, are too high in energy to be thermodynamically significant.) The γ formulation, however, has too high a transition temperature. This error arises because the probability that the cluster is in the solid-like state derived from quenching is higher than the corresponding probability derived from the STA temperature distributions. In the γ formulation the probabilities, p_i, at E' are

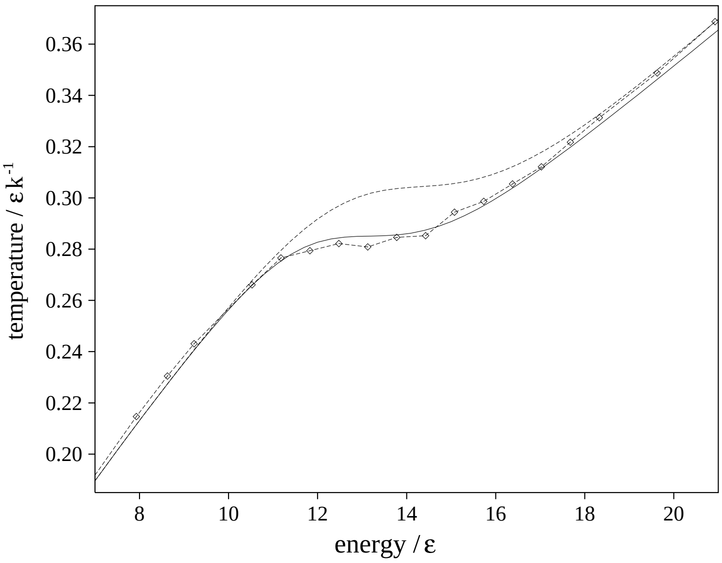

Figure 3.8: Microcanonical caloric curves for LJ_{13} using the n^* formula (solid line), the γ formula (dashed line) and from simulation (dashed line with diamonds). Both the n^* and γ formula curves include anharmonic terms.

fixed by the quench statistics (equation 3.31), and so this constraint leads to the higher transition temperature. The difference between the probabilities derived from quenching and the STA temperature distributions may be because there are regions of the PES which are in the basin of attraction of the icosahedron but which have thermodynamic properties similar to a liquid-like well, or because the short-time averaging does not distinguish between the solid-like and liquid-like states with the same resolution as for LJ_{55}. This difference does not stem from the quench method since we obtained similar quench statistics with steepest-descent[170,171], conjugate gradient[87] and eigenvector-following[88] methods.

3.6 Thermodynamic Properties

The accurate expressions for $\Omega(E)$ developed in the previous section can be used to give a wide range of thermodynamic functions, in fact, all except those that depend on derivatives of N or V. The exceptions arise because the thermodynamic properties of small clusters are discontinuously dependent on N and because the volume of a cluster is hard to define[172]. The formulae for the functions illustrated in this section are given in the appendix. They have, for the most part, been derived in previous work within the harmonic approximation[153,133]; the extension to incorporate anharmonicity follows simply from the expressions given in the

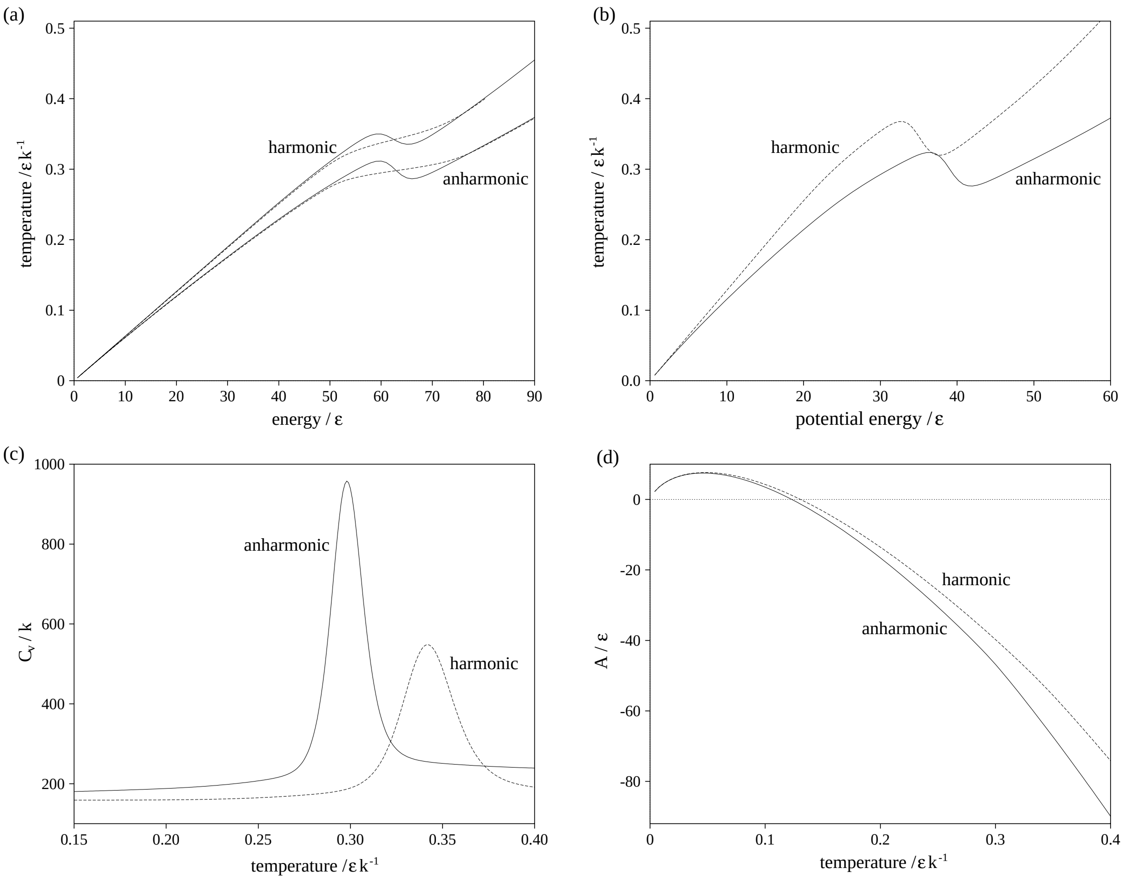

FIGURE 3.9: Comparison of harmonic and anharmonic thermodynamic functions of LJ_{55}: (a) the microcanonical (solid line) and canonical (dashed line) caloric curves, (b) the isopotential caloric curve, (c) $C_v(T)$ and (d) $A(T)$. In all except (a) the anharmonic curve is denoted by a solid line and the harmonic by a dashed line. Energies are measured with respect to the global minimum icosahedron.

previous section. The results are given for the most accurate partition functions: the first-order corrected γ formula for LJ_{55} using sample A and the second-order corrected n^* formula for LJ_{13} using sample D.

Harmonic and anharmonic results for the caloric curves, the heat capacity C_v, the Helmholtz free energy A, the transition temperature $T_{\frac{1}{2}}$ and the latent heat L_m are compared in Figures 3.9 and 3.10 and Table 3.8. We define $T_{\frac{1}{2}}$ as the temperature for which the two states have an equal Landau free energy, $A_L(E_c)$. L_m is the internal energy difference between the two states at $T_{\frac{1}{2}}$ and was obtained by extrapolating the caloric curves for each state to $T_{\frac{1}{2}}$ using equation 3.29. For LJ_{13}, this procedure simply gives $L_m = U_{II} - U_I$, where U_i is the internal energy of region i. For LJ_{55}, we have used $L_m = U_{V-VI} - U_{I-IV}$, where U_{I-IV} is the internal energy for the region of the PES formed from the combination of regions

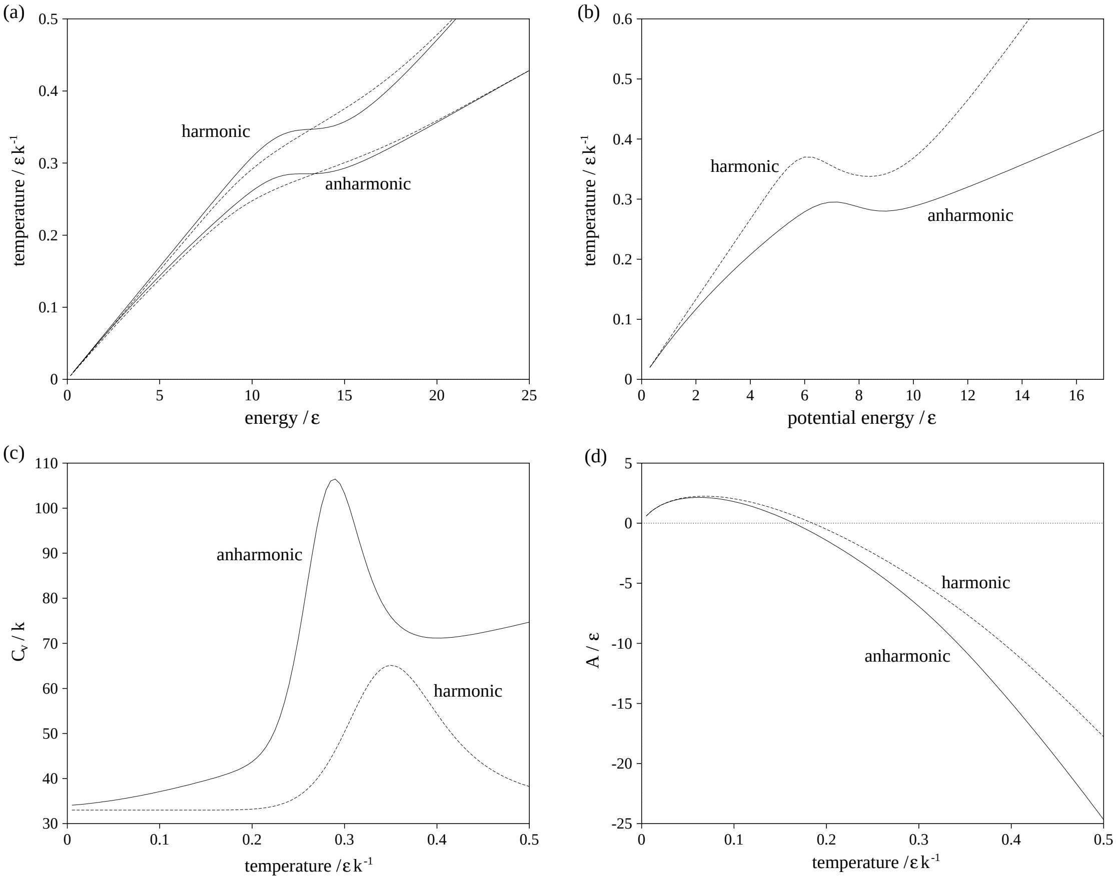

FIGURE 3.10: Comparison of harmonic and anharmonic thermodynamic functions of LJ_{13}: (a) the microcanonical (solid line) and canonical (dashed line) caloric curves, (b) the isopotential caloric curve, (c) $C_v(T)$ and (d) $A(T)$. In all except (a) the anharmonic curve is denoted by a solid line and the harmonic by a dashed line. Energies are measured with respect to the global minimum icosahedron.

I-IV, and so L_m does not include the latent heat associated with the disordering of the surface that occurs before melting. Just integrating C_v over the transition region would overestimate L_m because it would also include the energy needed to raise the temperature of the cluster.

The anharmonic caloric curves are displaced downward and away from their harmonic equivalents because of the increased densities of states associated with higher potential energy, lower temperature regions of the PES. The anharmonic heat capacity curve of LJ_{55} is in very good agreement with results from the multi-histogram MC[135] and J-walking[173] simulations. The peak in the heat capacity curve is larger and sharper when anharmonicity is included. This change can be understood by considering a two level system, which is a reasonable model to describe the equilibrium between solid-like and liquid-like states of the cluster.

TABLE 3.8: Transition temperatures and latent heats for LJ_{13} and LJ_{55}.

	LJ_{13}	LJ_{55}
$T_{\frac{1}{2}}/\epsilon\, k^{-1}$ (anharmonic)	0.2869	0.2985
$T_{\frac{1}{2}}/\epsilon\, k^{-1}$ (harmonic)	0.3512	0.3427
L_m/ϵ (anharmonic)	3.696	15.821
L_m/ϵ (harmonic)	2.887	12.837

The partition function can be written as $Z = \sum_i Z_i$, where the sum is over the two distinct regions of phase space. It follows that

$$U = -\left(\frac{\partial \ln Z}{\partial \beta}\right)_{N,V} = -\frac{1}{Z}\sum_i \left(\frac{\partial Z_i}{\partial \beta}\right)_{N,V} = \sum_i p_i U_i, \tag{3.40}$$

where $p_i = Z_i/Z$ and $U_i = -(\partial \ln Z_i/\partial \beta)_{N,V}$. Hence,

$$\begin{aligned} C_v &= \left(\frac{\partial U}{\partial T}\right)_{N,V} = \sum_i \left(p_i C_{v,i} + U_i \left(\frac{\partial p_i}{\partial T}\right)_{N,V}\right) && (3.41) \\ &= \frac{1}{2}(C_{v,1} + C_{v,2}) + L_m \left(\frac{\partial p_2}{\partial T}\right)_{N,V} \quad \text{when} \quad p_1 = p_2 = \frac{1}{2}, && (3.42) \end{aligned}$$

where $L_m = U_2(T_{\frac{1}{2}}) - U_1(T_{\frac{1}{2}})$ and $C_{v,i} = (\partial U_i/\partial T)_{N,V}$. As

$$\left(\frac{\partial p_i}{\partial T}\right)_{N,V} = \frac{1}{kT^2}\left(\frac{Z_i}{Z^2}\left(\frac{\partial Z}{\partial \beta}\right)_{N,V} - \frac{1}{Z}\left(\frac{\partial Z_i}{\partial \beta}\right)_{N,V}\right) = \frac{p_i}{kT^2}(U_i - U), \tag{3.43}$$

$$\begin{aligned} \left(\frac{\partial p_2}{\partial T}\right)_{N,V} &= \frac{p_1 p_2}{kT^2}(U_2 - U_1) && (3.44) \\ &= \frac{L_m}{4kT_{\frac{1}{2}}^2} \quad \text{when} \quad p_1 = p_2 = \frac{1}{2}. && (3.45) \end{aligned}$$

Substituting this result into equation 3.42 gives

$$C_v = \frac{1}{2}(C_{v,1} + C_{v,2}) + \frac{L_m^2}{4kT_{\frac{1}{2}}^2}. \tag{3.46}$$

The greater anharmonicity of liquid-like minima causes L_m to be larger when anharmonicity is included. This change has two effects: it increases the area under the heat capacity peak, and causes the cluster to change between the two states more rapidly with temperature, decreasing the width of the peak.

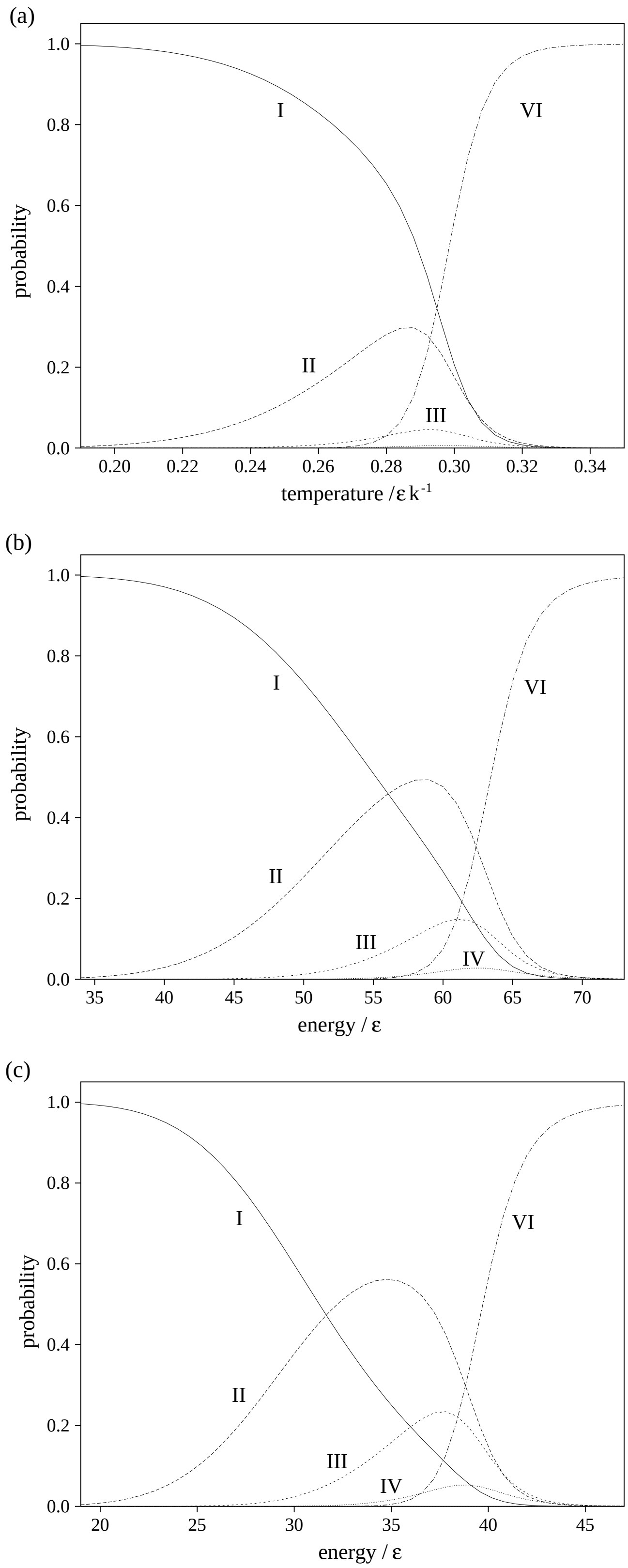

Figure 3.11: Probabilities of LJ_{55} being in regions I, II, III, IV and VI of the PES for (a) canonical, (b) microcanonical and (c) isopotential ensembles.

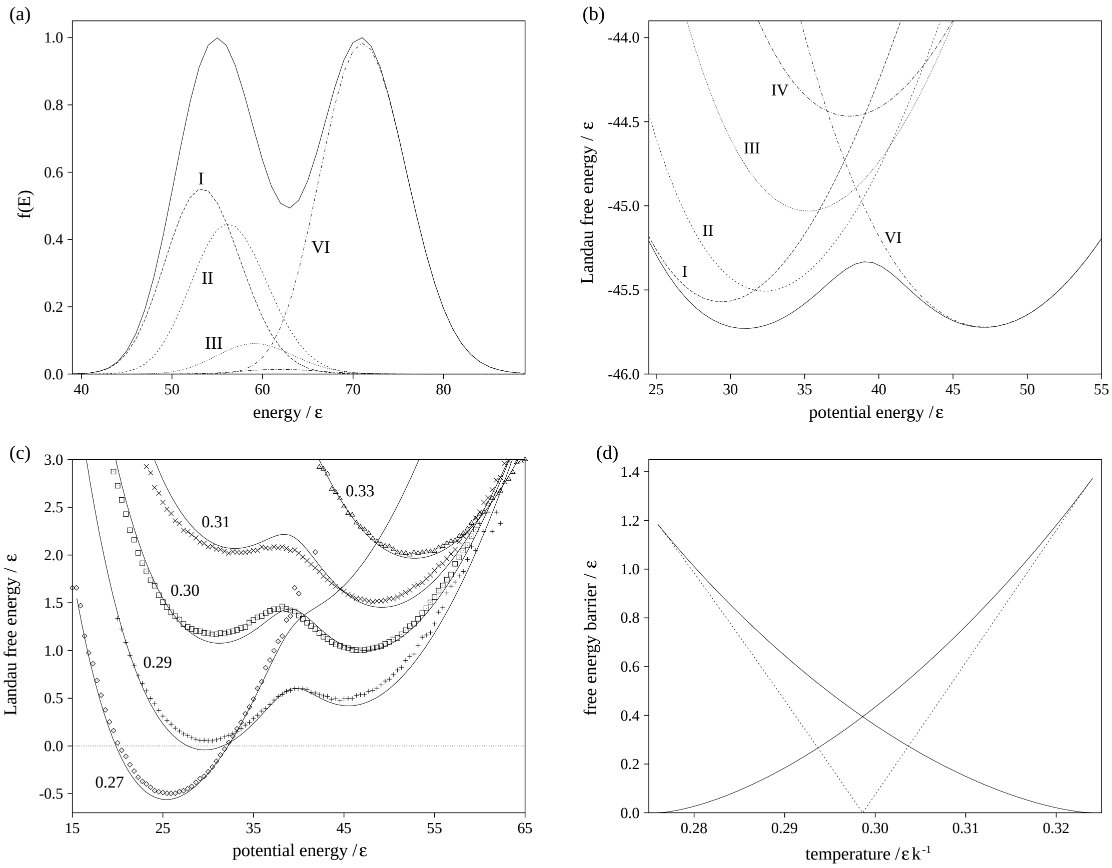

FIGURE 3.12: Plots for LJ_{55} of (a) $\mathcal{P}(E)$ at T=0.2985, (b) $A_L(E_c)$ at T=0.2985 (c) $A_L(E_c)$ at a number of temperatures as labelled and (d) the free energy barrier heights (solid lines) and the free energy difference between solid-like and liquid-like states (dashed line) for $A_L(E_c)$. In (a) and (b) the contributions of the different regions of the PES are also indicated. In (c) the results from our analytic partition function (solid line) are compared to simulation results (data points)[133].

From Figure 3.11 it can be seen that the probability of LJ_{55} being in regions II and III is lowest in the canonical ensemble and highest in the isopotential ensemble. This result is due to the dependence of the partition function on the independent variables, T, E and E_c, of the three ensembles. In the canonical ensemble, Z is exponentially dependent on T, and is the most steeply varying of the three partition functions. In the microcanonical and isopotential ensembles, Ω and Ω_c are dependent on powers of E and E_c, respectively. As the exponent of E_c is lower than that for E, Ω_c is the slowest varying of the partition functions. For LJ_{55} $n_I/n_{II-III} \gg n_{II-III}/n_{VI}$ (Table 3.9), where n_I, n_{II-III} and n_{VI} are the number of minima in regions I, II–III and VI, respectively. Consequently, as the partition function becomes more steeply varying, the defective icosahedra are seen for a

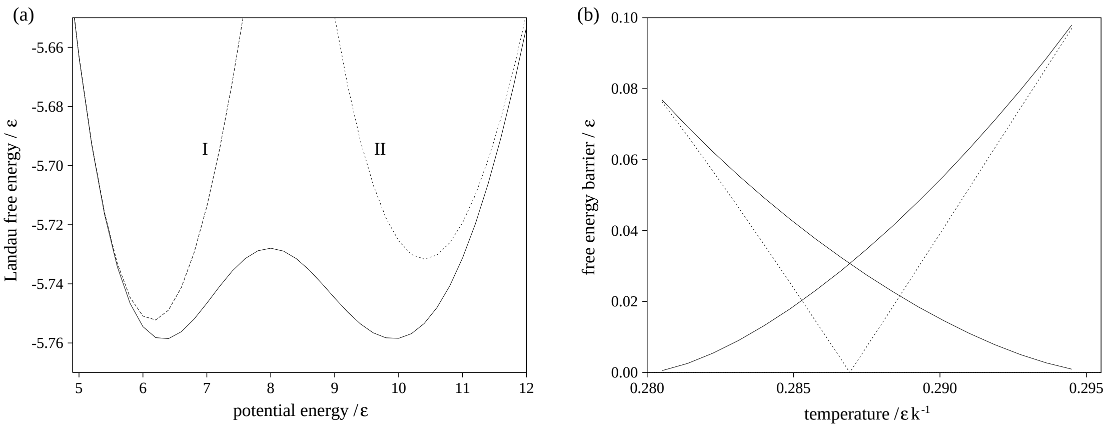

FIGURE 3.13: Plots for LJ_{13} of (a) $A_L(E_c)$ at T=0.2869, and (b) the free energy barrier heights (solid lines) and the free energy difference between solid-like and liquid-like states (dashed line) for $A_L(E_c)$. In (a) the contributions of liquid-like and solid-like states are shown.

narrower range of the independent variable, i.e. the contribution of the liquid-like states overtakes the defective icosahedra at an earlier stage in the generation of surface defects.

The Landau free energy, $A_L(Q)$, is the free energy of a system for a particular value of an order parameter Q. It is defined by

$$A_L(Q) = A - kT \ln p_Q(Q), \tag{3.47}$$

where $p_Q(Q)$ is the canonical probability distribution of the order parameter. The presence of two minima in $A_L(Q)$ indicates that there are two thermodynamically stable states at this temperature. As A is independent of Q, knowledge of $p_Q(Q)$ is sufficient to calculate the Landau free energy barrier. When E_c is used as an order parameter, simulations have shown that LJ_{55} has two Landau free energy minima which correspond to the solid-like and liquid-like states[133]. Bimodality in the canonical energy distribution function, $\mathcal{P}(E)$, implies that there are two Landau free energy minima as a function of the order parameter, E. Figures 3.12 and 3.13 show that both LJ_{13} and LJ_{55} have a range of temperature for which two Landau free energy minima are observed. As can be seen from 3.12c the predicted free energy curves for LJ_{55} are in very good agreement with those from simulation[133], confirming the accuracy of our analytic partition function. The states corresponding to the Mackay icosahedron and the defective icosahedra all contribute to the low potential energy minimum of $A_L(E_c)$, but the free energies of regions IV and V are never low enough to affect the thermodynamics. Although

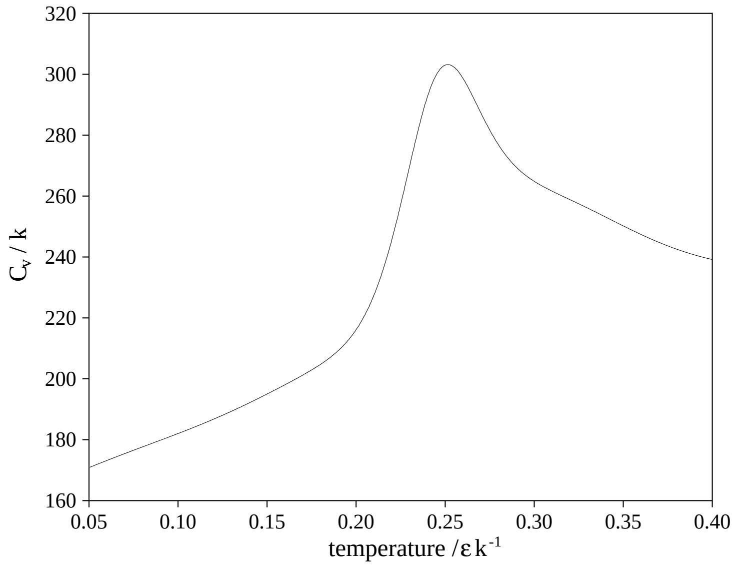

FIGURE 3.14: Heat capacity of LJ_{55} when only regions V and VI are included in the partition function.

the free energy barrier for LJ_{13} is much smaller, it has been observed in some simulations[142,174].

The turning points in $A_L(E_c)$ and $\mathcal{P}(E)$ correspond to points on the isopotential and the microcanonical caloric curves, respectively. This can be demonstrated for $A_L(E_c)$ by solving the equation $(\partial A_L/\partial E_c)_{N,V} = 0$. The solution is $1/kT = (\partial \ln \Omega_c/\partial E_c)_{N,V}$, which is simply the definition of the isopotential temperature. The maxima in $A_L(E_c)$ correspond to the segment of the caloric curve with negative slope, and the minima to segments with positive slope. Therefore the temperature range for which $A_L(E_c)$ has two minima is the same as the depth of the Van der Waals loop in the isopotential caloric curve, as can be seen by comparing Figures 3.9b and 3.12d, and 3.10b and 3.13b.

Comparing the results for LJ_{13} and LJ_{55} the effects of size are apparent. For LJ_{55} the melting transition is much more pronounced: it has a sharper peak in C_v, more pronounced Van der Waals loops in the microcanonical and isopotential caloric curves, a larger Landau free energy barrier, a larger temperature range for which solid-like and liquid-like clusters coexist, a larger latent heat per atom and a higher melting temperature. This behaviour is closer to the first-order phase transition of bulk matter.

One feature of the superposition method is that it allows one to restrict the regions of configuration space considered, and hence to look at thermodynamic properties which would be difficult to obtain by other methods. For example, we

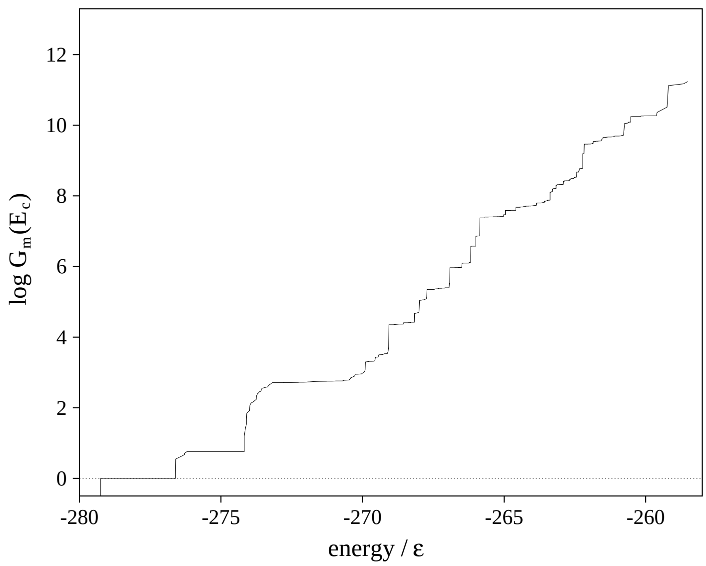

FIGURE 3.15: Plot of $G_m(E_c)$ for LJ_{55} as a function of the potential energy calculated using sample B.

can study the thermodynamic effects of structural relaxation in the absence of a transition to the solid-like state, thus enabling us to study supercooled liquid-like and perhaps even glass-like clusters. This could not easily be done by simulation since for LJ_{55} the cluster readily passes into the solid-like region of configuration space on cooling. Shown in Figure 3.14 is $C_{v,V-VI}$, the heat capacity when only regions V and VI are included in the partition function. It shows a clear peak at T=0.252 ($0.84T_{\frac{1}{2}}$), which has a height above the background C_v that is about a seventh of that for melting. It resembles the heat capacity peak that is often seen at the bulk glass transition. Such an interpretation should be caveated by the fact that the peak is dependent on where one decides the low energy tail of the liquid-like minima finishes.

Estimates of the number of minima in different regions of the PES can be obtained from the quench frequencies. Using equations 3.6, 3.7 and 3.9 an expression for g_s can be derived:

$$g_s = \frac{\gamma(E')_s h_s \prod_{j=1}^{\kappa} \nu_j^s}{\gamma(E')_0 h_0 \prod_{j=1}^{\kappa} \nu_j^0} \sum_{l=0}^{\kappa} \frac{C_l^\kappa a_0^l (E' - E_0^0)^{\kappa+l-1}}{\Gamma(\kappa+l)} \Bigg/ \sum_{l=0}^{\kappa} \frac{C_l^\kappa a_s^l (E' - E_s^0)^{\kappa+l-1}}{\Gamma(\kappa+l)}. \quad (3.48)$$

From g_s, the sum of minima, $G_m(E_c)$, can easily be calculated

$$G_m(E_c) = \sum_{E_s^0 < E_c} g_s. \quad (3.49)$$

This approach has been applied to LJ_{55}. From Figure 3.15 it can be seen that above -270ϵ the number of minima rises exponentially with the energy. The total

TABLE 3.9: Estimated numbers of geometrically distinct minima of LJ_{55} in the six energy ranges given in Table 3.1 calculated using sample A.

Region	number of minima	
	anharmonic	harmonic
I	1	1
II	11.3	6.3
III	994.6	457.9
IV	81.5	2871.2
V	1.26×10^5	1.22×10^6
VI	8.30×10^{11}	3.11×10^{12}

number of minima in the energy range probed by the MD quenching (potential energies up to -259ϵ) is 8.3×10^{11}. This value is much less than the total number of minima predicted by extrapolating Tsai and Jordan's results for small clusters and so suggests that the number of minima will continue to rise exponentially above -259ϵ. The present method has also been used to estimate the number of minima in the energy ranges I-VI (Table 3.9). The number of minima in range II is known[108] to be 11. The results from the quench frequencies agree well with this figure.

The methods developed here should be applicable to other types of clusters, although, as in our examples, the most appropriate form for the anharmonic terms may depend on the type and size of cluster considered. The advantages of the superposition method are that once the partition function is obtained it can be used to calculate a whole gamut of thermodynamic properties analytically, and that it allows one to consider the roles of different regions of configuration space and so gain more physical insight into the system, particularly the relationship between structure and thermodynamics. (If one simply wants $\Omega(E)$ without these extras, one should use a simulation method, such as multi-histogram MC[141].) However, the method currently relies upon there being an energy at which all relevant regions of phase space are sampled. This condition does not hold for larger clusters, such as LJ_{147}. To extend the method to such systems an analogue of the multi-histogram technique would need to be developed, in which the information from quenching at different energies could be combined. The expressions for the density of states could also be used to calculate accurate rate constants using RRKM (Rice-Ramsperger-Kassel-Marcus) theory[166,175], and so aid quantitative elucidation of dynamic properties from a knowledge of the transition states on the PES.

3.7 Van der Waals Loops and Size Dependence

Here, building upon previous work[134], we consider the conditions for a Van der Waals loop to occur in the microcanonical caloric curve using a two state model. By differentiating equation 3.30, we obtain

$$\left(\frac{\partial T}{\partial E}\right)_{N,V} = T^2 \sum_i \left[\frac{p_i}{T_i^2}\left(\frac{\partial T_i}{\partial E}\right)_{N,V} - \frac{1}{T_i}\left(\frac{\partial p_i}{\partial E}\right)_{N,V}\right], \tag{3.50}$$

where the probabilities and their derivatives obey $\sum_i p_i = 1$ and $\sum_i (\partial p_i/\partial E)_{N,V} = 0$. For a two state system, this expression becomes

$$\left(\frac{\partial T}{\partial E}\right)_{N,V} = T^2\left(\frac{\partial p_1}{\partial E}\right)_{N,V}\left(\frac{1}{T_2} - \frac{1}{T_1}\right) + T^2\left(\frac{p_1}{T_1^2}\left(\frac{\partial T_1}{\partial E}\right)_{N,V} + \frac{p_2}{T_2^2}\left(\frac{\partial T_2}{\partial E}\right)_{N,V}\right). \tag{3.51}$$

The first term in this expression is negative and the second positive (assuming region 1 has a lower potential energy than region 2). To exhibit a Van der Waals loop, the caloric curve must have a region of negative slope, and therefore the following inequality must be satisfied for some range of energy,

$$\left(\frac{\partial p_2}{\partial E}\right)_{N,V}\left(\frac{1}{T_2} - \frac{1}{T_1}\right) > \frac{p_1}{T_1^2}\left(\frac{\partial T_1}{\partial E}\right)_{N,V} + \frac{p_2}{T_2^2}\left(\frac{\partial T_2}{\partial E}\right)_{N,V}. \tag{3.52}$$

If we assume both regions behave harmonically, then $T_1 = \alpha E$ and $T_2 = \alpha(E-\Delta)$, where Δ is the potential energy difference between the minima of the two regions. This assumption gives

$$\left(\frac{\partial p_2}{\partial E}\right)_{N,V}\left(\frac{1}{E-\Delta} - \frac{1}{E}\right) \;>\; \frac{p_1}{E^2} + \frac{p_2}{(E-\Delta)^2}, \tag{3.53}$$

$$\text{so} \quad \left(\frac{\partial p_2}{\partial E}\right)_{N,V}\Delta \;>\; p_1\left(1-\frac{\Delta}{E}\right) + p_2\left(1-\frac{\Delta}{E}\right)^{-1},$$

$$\;>\; 1 + \frac{\Delta}{E}(p_2 - p_1) + O\left(\left(\frac{\Delta}{E}\right)^2\right). \tag{3.54}$$

In the middle of the coexistence region where $p_1 = p_2 = 1/2$, neglecting second order terms in (Δ/E) gives

$$\left(\frac{\partial p_2}{\partial E}\right)_{N,V}\Delta > 1. \tag{3.55}$$

This equation was previously derived by Bixon and Jortner[152] for Van der Waals loops in the kinetic temperature. We now continue the analysis, first noting that

$$\left(\frac{\partial p_i}{\partial E}\right)_{N,V} = \frac{1}{\Omega}\left(\frac{\partial \Omega_i}{\partial E}\right)_{N,V} - \frac{\Omega_i}{\Omega^2}\left(\frac{\partial \Omega}{\partial E}\right)_{N,V}, \tag{3.56}$$

$$= \frac{p_i}{k}\left(\frac{1}{T_i} - \frac{1}{T}\right). \tag{3.57}$$

Therefore, using equation 3.30

$$\left(\frac{\partial p_2}{\partial E}\right)_{N,V} = \frac{p_1 p_2}{k}\left(\frac{1}{T_2} - \frac{1}{T_1}\right) = \frac{p_1 p_2}{\alpha k}\frac{\Delta}{E(E-\Delta)}. \tag{3.58}$$

Substituting this result into equation 3.53 and rearranging gives

$$\left(p_1 - \frac{p_1 p_2}{\alpha k}\right)\left(\frac{\Delta}{E}\right)^2 - 2p_1\frac{\Delta}{E} + 1 < 0. \tag{3.59}$$

Taking the middle of the coexistence region, where $p_1 = p_2 = 1/2$ and $E = E_{\frac{1}{2}}$:

$$\left(1 - \frac{1}{2\alpha k}\right)\left(\frac{\Delta}{E_{\frac{1}{2}}}\right)^2 - 2\frac{\Delta}{E_{\frac{1}{2}}} + 2 < 0. \tag{3.60}$$

As this quadratic has negative curvature for all realistic values of α, the above inequality has a physically meaningful solution when $(\Delta/E_{\frac{1}{2}})$ is greater than the larger root of the quadratic. This solution is

$$\frac{\Delta}{E_{\frac{1}{2}}} > \frac{\left(\frac{1}{\alpha k} - 1\right)^{1/2} - 1}{\left(\frac{1}{2\alpha k} - 1\right)}. \tag{3.61}$$

For a single harmonic minimum of an N-atom cluster

$$\frac{1}{\alpha} = \left(\frac{\partial E}{\partial T}\right)_{N,V} = (3N-7)k. \tag{3.62}$$

Hence,

$$\frac{\Delta}{E_{\frac{1}{2}}} > \frac{2((3N-8)^{1/2}-1)}{(3N-9)} \approx \frac{2}{\sqrt{3N}} \qquad \text{for large } N. \tag{3.63}$$

A similar relationship can be derived for the N-dependence of Van der Waals loops in the caloric curve of the isopotential ensemble. In this case

$$\left(\frac{\partial E_c}{\partial T_c}\right)_{N,V} = \left(\frac{3N}{2} - 4\right)k, \tag{3.64}$$

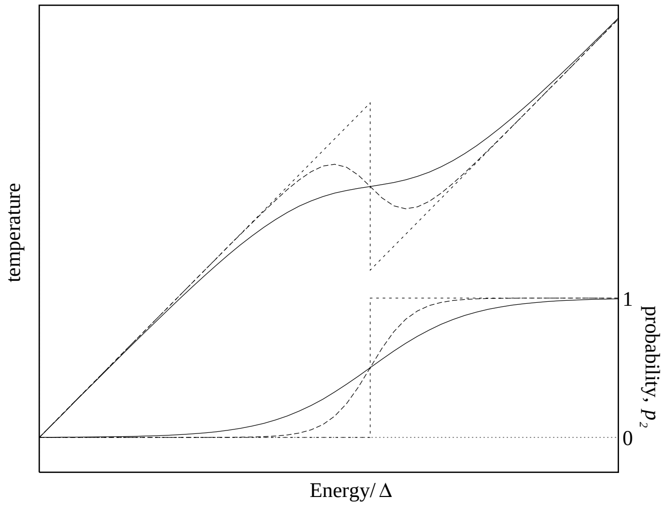

FIGURE 3.16: Plots of temperature (top) and probability, p_2, (bottom) for a two state system. $E_{\frac{1}{2}}/\Delta$ is kept constant as N is varied. The solid line is for small N, long dashed line is for intermediate N and the short dashed line for the bulk limit.

where E_c is the potential energy and T_c is the isopotential temperature. Hence,

$$\frac{\Delta}{E_{c,\frac{1}{2}}} > 2\sqrt{\frac{2}{3N}} \qquad \text{for large } N. \tag{3.65}$$

As $E_{c,\frac{1}{2}} < E_{\frac{1}{2}}/\sqrt{2}$, this confirms that a Van der Waals loop is more likely in the isopotential ensemble than the microcanonical ensemble. As we saw earlier, LJ_{13} has a Van der Waals loop in the isopotential caloric curve but not in the microcanonical curve.

From equation 3.63 it is clear that for a series of structures with similar values of $\Delta/E_{\frac{1}{2}}$, a Van der Waals loop will become more likely as the size increases (Figure 3.16). This result is in good agreement with simulations of icosahedral LJ[135] and cuboctahedral gold clusters[136].

In the bulk limit the above model predicts the caloric curve will be vertical at $E_{\frac{1}{2}}$ (Figure 3.16), which is clearly at variance with the expected behaviour for a bulk first-order phase transition. This discrepancy arises because we have not allowed for the cluster dividing into distinct solid-like and liquid-like regions, which would contribute a term of the form $\Omega_s^{(1-x)}\Omega_l^x$ to the density of states, where x is the fraction of the cluster that is liquid-like. Such phase separation does not occur for small clusters because the energy of the dividing surface makes it unfavourable, but for the bulk the interface is a negligible fraction of the total energy. Recently, an analytical model has been investigated which predicts the size evolution of the microcanonical caloric curve as phase separation becomes possible[176].

Equation 3.63 also shows us that a Van der Waals loop becomes more likely as the quantity $\Delta/E_{\frac{1}{2}}$ increases. We can understand the conditions for this quantity to be large by considering the density of states for each region. For simplicity we do this within the harmonic approximation. We consider region 1 to be made up of n_1 similar geometric isomers (with the same energy, vibrational frequencies and point group), and region 2 of n_2. Each geometric isomer has $2N!/h_i$ permutational isomers. These assumptions yield

$$\Omega_1 = \frac{2n_1 N! E^{\kappa-1}}{h_1 \Gamma(\kappa)(h\overline{\nu}_1)^\kappa} \quad \text{and} \quad \Omega_2 = \frac{2n_2 N!(E-\Delta)^{\kappa-1}}{h_2 \Gamma(\kappa)(h\overline{\nu}_2)^\kappa}, \tag{3.66}$$

where h_i is the order of the point group for states in region i. $\Omega_1 = \Omega_2$ at $E = E_{\frac{1}{2}}$. Hence,

$$\frac{\Delta}{E_{\frac{1}{2}}} = \left(1 - \left(\frac{n_1 h_2 \overline{\nu}_2)^\kappa}{n_2 h_1 \overline{\nu}_1)^\kappa}\right)^{1/(\kappa-1)}\right). \tag{3.67}$$

From this expression we can see that $\Delta/E_{\frac{1}{2}}$ increases, making a Van der Waals loop more likely, as region 1 becomes more solid-like (a few high symmetry, rigid states) and as region 2 becomes more liquid-like (many low symmetry, non-rigid states).

Appendix: Thermodynamic Formulae

In this appendix, the formulae for some of the thermodynamic quantities that can be calculated by the superposition method are given. The thermodynamic functions are derived from the following definitions.

In the isopotential ensemble,

$$p_i(E_c) = \frac{\Omega_{c,i}(E_c)}{\Omega_c(E_c)}, \qquad \frac{1}{kT_c(E_c)} = \left(\frac{\partial \ln \Omega_c}{\partial E_c}\right)_{N,V}.$$

In the microcanonical ensemble,

$$p_i(E) = \frac{\Omega_i(E)}{\Omega(E)}.$$

In the canonical ensemble,

$$p_i(T) = \frac{Z_i}{Z},$$

$$U(T) = -\left(\frac{\partial \ln Z}{\partial \beta}\right)_{N,V} = \frac{1}{Z_{0,0}}(Z_{1,0} + Z_{0,1}),$$

$$
\begin{aligned}
C_v(T) &= \left(\frac{\partial U}{\partial T}\right)_{N,V}, \\
&= \frac{1}{kT^2}\left(\frac{1}{Z_{0,0}}(Z_{2,0}+2Z_{1,1}+Z_{0,2}) - \left(\frac{Z_{1,0}+Z_{0,1}}{Z_{0,0}}\right)^2\right),
\end{aligned}
$$

$$A(T) = E_0^0 - kT\ln Z,$$

$$\mathcal{P}(E) = \Omega(E)\exp(-\beta E),$$

$$A_L(E_c) = E_c - kT\ln\Omega_c(E_c),$$

where in $Z_{\alpha,\delta}$ the derivative of the exponential function of β in Z has been taken α times and the derivative of the inverse power of β in Z δ times. Therefore, $Z = Z_{0,0}$.

Below, we give the thermodynamic functions for the γ formulation with a first-order anharmonic correction which was used for LJ_{55}.

$$
T_c(E_c) = \frac{\displaystyle\sum_{E_s^0<E_c}\gamma(E')_s \sum_{l=0}^{\kappa}\frac{C_l^\kappa a_s^l (E_c-E_s^0)^{\kappa/2+l-1}}{\Gamma(\kappa/2+l)}\Big/\sum_{l=0}^{\kappa}\frac{C_l^\kappa a_s^l(E'-E_s^0)^{\kappa+l-1}}{\Gamma(\kappa+l)}}{\displaystyle k\sum_{E_s^0<E_c}\gamma(E')_s \sum_{l=0}^{\kappa}\frac{C_l^\kappa a_s^l (E_c-E_s^0)^{\kappa/2+l-2}}{\Gamma(\kappa/2+l-1)}\Big/\sum_{l=0}^{\kappa}\frac{C_l^\kappa a_s^l(E'-E_s^0)^{\kappa+l-1}}{\Gamma(\kappa+l)}}.
$$

$$
Z_{\alpha,\delta} = c\sum_s \gamma(E')_s (E_s^0)^\alpha e^{-\beta E_s^0}\sum_{l=0}^{\kappa}\frac{\Gamma(\kappa+l+\delta)}{\Gamma(\kappa+l)}\frac{C_l^\kappa a_s^l}{\beta^{\kappa+l+\delta}}\Big/\sum_{l=0}^{\kappa}\frac{C_l^\kappa a_s^l(E'-E_s^0)^{\kappa+l-1}}{\Gamma(\kappa+l)}.
$$

$$
A_L(E_c) = E_c - \frac{1}{\beta}\ln\frac{c}{\beta^{\kappa/2}}\sum_{E_s^0<E_c}\gamma(E')_s\sum_{l=0}^{\kappa}\frac{C_l^\kappa a_s^l(E_c-E_s^0)^{\kappa/2+l-1}}{\Gamma(\kappa/2+l)}\Big/\sum_{l=0}^{\kappa}\frac{C_l^\kappa a_s^l(E'-E_s^0)^{\kappa+l-1}}{\Gamma(\kappa+l)},
$$

where

$$
c = \frac{n_0^*}{\gamma(E')_0\prod_{j=1}^{\kappa}h\nu_j^0}\sum_{l=0}^{\kappa}\frac{C_l^\kappa a_0^l(E'-E_0^0)^{\kappa+l-1}}{\Gamma(\kappa+l)}.
$$

The harmonic forms can be recovered by taking the $l=0$ term. We obtain the n^* formulation by replacing

$$
c\,\gamma(E')_s\Big/\sum_{l=0}^{\kappa}\frac{C_l^\kappa a_s^l(E'-E_s^0)^{\kappa+l-1}}{\Gamma(\kappa+l)} \qquad \text{with} \qquad \frac{n_s^*}{\prod_{j=1}^{\kappa}h\nu_j^s}.
$$

Below, we give the thermodynamic functions for the n^* formulation with second-order anharmonic corrections which was used for LJ_{13}.

$$
T_c(E_c) = \frac{\displaystyle\sum_{E_s^0<E_c}\frac{n_s^*}{\prod_{j=1}^{\kappa}h\nu_j^s}\sum_{l=0}^{\kappa}\sum_{m=0}^{\kappa-l}\frac{D_{l,m}^\kappa 3^m a_s^{l+2m}(E_c-E_s^0)^{\kappa/2+l+2m-1}}{\Gamma(\kappa/2+l+2m)}}{\displaystyle k\sum_{E_s^0<E_c}\frac{n_s^*}{\prod_{j=1}^{\kappa}h\nu_j^s}\sum_{l=0}^{\kappa}\sum_{m=0}^{\kappa-l}\frac{D_{l,m}^\kappa 3^m a_s^{l+2m}(E_c-E_s^0)^{\kappa/2+l+2m-2}}{\Gamma(\kappa/2+l+2m-1)}},
$$

$$Z_{\alpha,\delta} = \sum_s \frac{n_s^* e^{-\beta E_s^0} (E_s^0)^\alpha}{\prod_{j=1}^\kappa h\nu_j^s} \sum_{l=0}^{\kappa} \sum_{m=0}^{\kappa-l} \frac{\Gamma(\kappa+l+2m+\delta)}{\Gamma(\kappa+l+2m)} \frac{D_{l,m}^\kappa 3^m a_s^{l+2m}}{\beta^{\kappa+l+2m+\delta}},$$

$$A_L(E_c) = E_c - \frac{1}{\beta} \ln \sum_{E_s^0 < E_c} \frac{n_s^*}{\beta^{\kappa/2} \prod_{j=1}^\kappa h\nu_j^s} \sum_{l=0}^{\kappa} \sum_{m=0}^{\kappa-l} \frac{D_{l,m}^\kappa 3^m a_s^{l+2m} (E_c - E_s^0)^{\kappa/2+l+2m-1}}{\Gamma(\kappa/2+l+2m)}.$$

The harmonic forms can be recovered by taking the $l = 0, m = 0$ term, and the first-order correction forms by taking the $m = 0$ terms. We obtain the γ formulation by replacing

$$\frac{n_s^*}{\prod_{j=1}^\kappa h\nu_j^s} \qquad \text{with} \qquad c\,\gamma(E')_s \Bigg/ \sum_{l=0}^{\kappa} \sum_{m=0}^{\kappa-l} \frac{D_{l,m}^\kappa 3^m a_s^{l+2m} (E' - E_s^0)^{\kappa+l+2m-1}}{\Gamma(\kappa+l+2m)},$$

where

$$c = \frac{n_0^*}{\gamma(E')_0 \prod_{j=1}^\kappa h\nu_j^0} \sum_{l=0}^{\kappa} \sum_{m=0}^{\kappa-l} \frac{D_{l,m}^\kappa 3^m a_0^{l+2m} (E' - E_0^0)^{\kappa+l+2m-1}}{\Gamma(\kappa+l+2m)}.$$